AD-A174 968 COMPUTATION OF THREE DIMENSIONAL VISCOUS COMPRESSIBLE FLOW AT HYPERSONIC..(U) STANFORD UNIV CA DEPT OF AERONAUTICS AND ASTRONAUTICS G V CANDLER ET AL. 1/1

UNCLASSIFIED 01 SEP 86 AFOSR-TR-86-2098 AFOSR-85-0372 F/G 20/4 NL

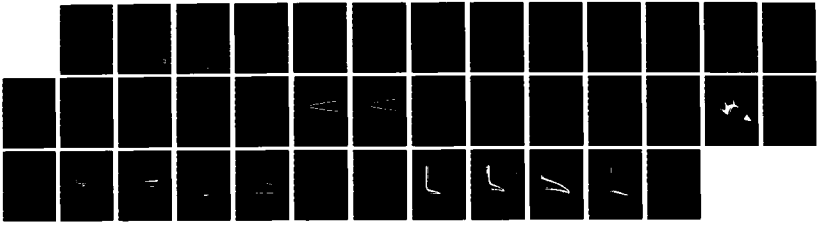

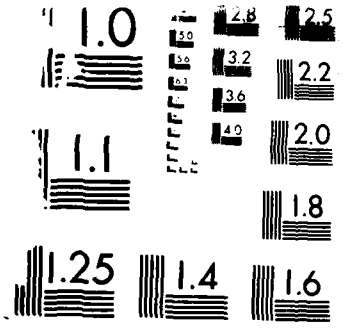

RESOLUTION TEST CHART

Department of AERONAUTICS and ASTRONAUTICS
STANFORD UNIVERSITY

FINAL REPORT

AFOSR-85-0372

COMPUTATION OF THREE DIMENSIONAL VISCOUS COMPRESSIBLE FLOW AT HYPERSONIC VELOCITY

submitted to

Dr. James Wilson, Program Manager
Room A223, Directorate of Aerospace Sciences
AIR FORCE OFFICE OF SCIENTIFIC RESEARCH
Bolling Air Force Base, D.C. 20332

by

Department of Aeronautics and Astronautics
STANFORD UNIVERSITY
Stanford, CA 94305

Professor R.W. MacCormack
Principal Investigator

September 1986

UNCLASSIFIED

SECURITY CLASSIFICATION OF THIS PAGE

AD-A174 968

REPORT DOCUMENTATION PAGE

Form Approved
OMB No. 0704-0188
Exp. Date: Jun 30, 1986

1a. REPORT SECURITY CLASSIFICATION	1b. RESTRICTIVE MARKINGS
2a. SECURITY CLASSIFICATION AUTHORITY	3. DISTRIBUTION/AVAILABILITY OF REPORT
2b. DECLASSIFICATION/DOWNGRADING SCHEDULE	Approved for public release; distribution unlimited.
4. PERFORMING ORGANIZATION REPORT NUMBER(S) AFOSR 85 0372	5. MONITORING ORGANIZATION REPORT NUMBER(S) AFOSR-TR- 86-2028
6a. NAME OF PERFORMING ORGANIZATION STANFORD UNIVERSITY 6b. OFFICE SYMBOL (If applicable)	7a. NAME OF MONITORING ORGANIZATION AFOSR
6c. ADDRESS (City, State, and ZIP Code) Stanford, CA 94305-2028	7b. ADDRESS (City, State, and ZIP Code) Air Force Office of Scientific Research Bolling Air Force Base, D.C. 20332
8a. NAME OF FUNDING/SPONSORING ORGANIZATION AFOSR 8b. OFFICE SYMBOL (If applicable) AFOSR/NA	9. PROCUREMENT INSTRUMENT IDENTIFICATION NUMBER AFOSR-85-0372
8c. ADDRESS (City, State, and ZIP Code) Air Force Office of Scientific Research Bolling Air Force Base, D.C. 20332	10. SOURCE OF FUNDING NUMBERS PROGRAM ELEMENT NO. 61102F; PROJECT NO. 2307; TASK NO. A1; WORK UNIT ACCESSION NO.

11. TITLE (Include Security Classification)
COMPUTATION OF THREE DIMENSIONAL VISCOUS COMPRESSIBLE FLOW AT HYPERSONIC VELOCITY
~~HYPERSONIC FLOW PAST 3-D CONFIGURATIONS~~

12. PERSONAL AUTHOR(S)
Graham V. Candler and Robert W. MacCormack

13a. TYPE OF REPORT	13b. TIME COVERED	14. DATE OF REPORT (Year, Month, Day)	15. PAGE COUNT
Final	FROM 10/1/85 TO 9/30/86	1986, 9, 1	35

16. SUPPLEMENTARY NOTATION

17 COSATI CODES			18. SUBJECT TERMS (Continue on reverse if necessary and identify by block number)
FIELD	GROUP	SUB-GROUP	

19. ABSTRACT (Continue on reverse if necessary and identify by block number)

A numerical method to solve the perfect gas Navier-Stokes equations for the hypersonic flows past three-dimensional blunt bodies has been developed. The numerical method uses flux-splitting and shock-fitting with an implicit Gauss-Seidel line-relaxation procedure to accelerate convergence. The technique has been used to solve the flow field over a spherically blunted biconic and the X24C-10D hypersonic research vehicle. The method has been shown to reduce the number of iterations required to achieve convergence of a typical problem by a factor of about one hundred over an explicit method. The scheme also shows a potential advantage over approximately factored implicit methods. The key advantage of this technique is that the low number of iterations required for convergence does not increase as mesh resolution is refined.

20. DISTRIBUTION/AVAILABILITY OF ABSTRACT	21. ABSTRACT SECURITY CLASSIFICATION
☒ UNCLASSIFIED/UNLIMITED ☐ SAME AS RPT. ☐ DTIC USERS	202-767-4935
22a. NAME OF RESPONSIBLE INDIVIDUAL ~~Robert W. MacCormack~~ DR JAMES D WILSON	22b. TELEPHONE (Include Area Code) ~~(415) 723-3087~~
	22c. OFFICE SYMBOL ~~AFOSR/NA~~ NA

DD FORM 1473, 84 MAR 83 APR edition may be used until exhausted.
All other editions are obsolete.

SECURITY CLASSIFICATION OF THIS PAGE

UNCLASSIFIED

HYPERSONIC FLOW PAST 3-D CONFIGURATIONS

Graham V. Candler[1]
and
Robert W. MacCormack[2]
Department of Aeronautics and Astronautics
Stanford University
Stanford, CA

Abstract

A numerical method to solve the perfect gas Navier-Stokes equations for hypersonic flows past three-dimensional blunt bodies has been developed. The numerical method uses flux-splitting and shock-fitting with an implicit Gauss-Seidel line-relaxation procedure to accelerate convergence. The technique has been used to solve the flow field over a spherically blunted biconic and the X24C-10D hypersonic research vehicle. The method has been shown to reduce the number of iterations required to achieve convergence of a typical problem by a factor of about one hundred over an explicit method. The scheme also shows a potential advantage over approximately factored implicit methods. The key advantage of this technique is that the low number of iterations required for convergence does not increase as mesh resolution is refined.

Nomenclature

A, B, C	= Jacobians of F, G and H
c	= local speed of sound
c_p	= specific heat at constant pressure
c_v	= specific heat at constant volume
e	= total energy per unit mass
ei	= internal energy per unit mass, $ei = c_v T$
F, G, H	= flux vectors of the conserved flow variables
$\vec{F}$	= vector form of the flux components
i, j, k	= mesh coordinates in the ξ, η, ς directions
I, J, K	= largest values of the mesh coordinates
k, k_t	= molecular and eddy conductivity of the fluid
M	= Mach number
n	= time level of computation
p	= pressure
Pr, Pr_t	= Prandtl number and turbulent Prandtl number

[1]Graduate Student, Student Member AIAA
[2]Professor, Member AIAA

$\vec{\mathbf{q}}$ = heat flow vector
r_n = nose radius
$\vec{S}$ = surface normal vector
$S_{ix}, \cdots$ = x component of i surface normal vector, *etc.*
St = Stanton number, $St = |\vec{n} \cdot k\nabla T| / \rho_\infty u_\infty (c_p T_\infty + \frac{1}{2}u_\infty^2 - c_p T_{\text{wall}})$
t = time
T = temperature
u, v, w = x, y and z components of velocity
U = vector of conserved flow variables
V = cell volume
$\mathbf{V}$ = vector of the primitive flow variables
x, y, z = coordinate directions
y^+ = law of the wall variable
α = angle of attack
δU = implicit change in U, $\delta U^n \equiv U^{n+1} - U^n$
ΔU = explicit change in U, defined in Equation (7)
γ = ratio of specific heats
ξ, η, ζ = transformed coordinates
μ, μ_t = molecular and eddy viscosity coefficients
λ = bulk viscosity coefficient
ρ = fluid density
τ = shear stress tensor

Difference Operators

$$\frac{D_+ Z_{ijk}}{\Delta\xi} \equiv Z_{i+1jk} - Z_{ijk} \qquad \frac{D_- Z_{ijk}}{\Delta\xi} \equiv Z_{ijk} - Z_{i-1jk}$$
$$\frac{D_+ Z_{ijk}}{\Delta\eta} \equiv Z_{ij+1k} - Z_{ijk} \qquad \frac{D_- Z_{ijk}}{\Delta\eta} \equiv Z_{ijk} - Z_{ij-1k}$$
$$\frac{D_+ Z_{ijk}}{\Delta\zeta} \equiv Z_{ijk+1} - Z_{ijk} \qquad \frac{D_- Z_{ijk}}{\Delta\zeta} \equiv Z_{ijk} - Z_{ijk-1}$$

Introduction

The numerical solution of the three-dimensional Navier-Stokes equations is becoming commonplace and large complicated problems have been solved. A notable example is the solution of the flow field over an entire hypersonic aircraft performed by Shang and Scherr[1] in 1985. The numerical solution of the Navier-Stokes equations is a computationally intensive task requiring the full resources of a supercomputer. A typical problem may require on the order of 10^4 iterations to achieve a steady-state result when using an explicit algorithm. This is a result of the strict time step limitation imposed on the solution because of the fine mesh spacing needed near surfaces to resolve viscous and heat transfer effects. The Navier-Stokes equations also require a large number of calculations per time step to compute all of the terms in the equations. Thus the combination of these two factors leads to the use of much computer time to achieve a steady-state solution. A numerical method that reduces the number of iterations required to reach a steady-state or reduces the number of computations required per

iteration would enhance the ability to study flow physics using numerical solutions or allow more test cases to be run for a given amount of computer time.

In 1985 MacCormack[2] presented a numerical algorithm for the solution of the two-dimensional Navier-Stokes equations that demonstrates a large improvement in the number of iterations required for a steady-state result. The method was tested on several problems and a solution in less than twenty iterations was obtained for a two-dimensional transonic nozzle. The three-dimensional analog of this technique has been developed and tested; its characteristics and some test results from this method are presented here. The numerical method demonstrates several positive qualities, among which it:

- is fully conservative to prevent any numerical loss of mass, momentum or energy.
- is fully implicit, allowing large time steps to be taken.
- uses Gauss-Seidel line-relaxation to accelerate convergence.
- uses flux dependent differencing to maintain stability without having to introduce any smoothing terms into the difference equations.
- is second-order accurate in all spatial directions.
- uses shock-fitting to accurately capture the very strong gradients in the flow variables that occur at the bow shock wave.

However, the numerical method does have one main drawback, it requires many computations per time step, so that a large reduction in iterations converts to a smaller reduction in computer time. The results presented were obtained using a program that is not vectorized; a further reduction in computer time would be realized if vectorization was performed.

The numerical method has been tested on two configurations and the results compare well with previous experimental and computational work. The first body tested was a spherically blunted cone travelling at a Mach number of 7.97 and a Reynolds number of 1.2×10^8/m; angles of attack of between 0.0° and 7.0° were used. Secondly, the flow over the X24C-10D hypersonic research vehicle at a Mach number of 5.95, a characteristic Reynolds number of 16.4×10^6/m, and an angle of attack of 6.0° was computed. This is a duplication of the explicit efforts of Shang and Scherr, but using implicit Gauss-Seidel line-relaxation and shock-fitting. The use of the implicit method allowed a better resolution of the near wall viscous and heat transfer effects. The number of time steps required to achieve a steady-state solution for these problems is about a factor of one hundred less.

The Navier-Stokes Equations

The Navier-Stokes equations may be written as the integration over the surface of an arbitrary volume

$$\frac{\partial \vec{U}}{\partial t} + \frac{1}{V}\int_S \vec{F}\cdot d\vec{S} = 0, \tag{1}$$

where $\vec{U}$ is the vector of conserved variables averaged over the volume, $\vec{F}$ is the vector form of the fluxes of these conserved quantities, $\vec{F} = F\vec{i}_x + G\vec{i}_y + H\vec{i}_z$, and $d\vec{S}$ is the

differential surface vector of the volume. F, G, and H are the flux vectors expressed in Cartesian coordinates given below,

$$U = \begin{pmatrix} \rho \\ \rho u \\ \rho v \\ \rho w \\ e \end{pmatrix}, \qquad F = \begin{pmatrix} \rho u \\ \rho u^2 + p + \tau_{xx} \\ \rho uv + \tau_{xy} \\ \rho uw + \tau_{xz} \\ (e + p + \tau_{xx})u + \tau_{xy}v + \tau_{xz}w + q_x \end{pmatrix},$$

$$G = \begin{pmatrix} \rho v \\ \rho uv + \tau_{yx} \\ \rho v^2 + p + \tau_{yy} \\ \rho uw + \tau_{yz} \\ \tau_{yx}u + (e + p + \tau_{yy})v + \tau_{yz}w + q_y \end{pmatrix}, \qquad H = \begin{pmatrix} \rho w \\ \rho uw + \tau_{xz} \\ \rho uw + \tau_{zy} \\ \rho w^2 + p + \tau_{zz} \\ \tau_{zx}u + \tau_{zy}v + (e + p + \tau_{zz})w + q_z \end{pmatrix},$$

where,

$$\tau_{xx} = -2\tilde{\mu}\frac{\partial u}{\partial x} - \lambda\Big(\frac{\partial u}{\partial x} + \frac{\partial v}{\partial y} + \frac{\partial w}{\partial z}\Big), \qquad \tau_{xy} = \tau_{yx} = -\tilde{\mu}\Big(\frac{\partial u}{\partial y} + \frac{\partial v}{\partial x}\Big), \qquad q_x = -\tilde{k}\frac{\partial T}{\partial x},$$

$$\tau_{yy} = -2\tilde{\mu}\frac{\partial v}{\partial y} - \lambda\Big(\frac{\partial u}{\partial x} + \frac{\partial v}{\partial y} + \frac{\partial w}{\partial z}\Big), \qquad \tau_{xz} = \tau_{zx} = -\tilde{\mu}\Big(\frac{\partial u}{\partial z} + \frac{\partial w}{\partial x}\Big), \qquad q_y = -\tilde{k}\frac{\partial T}{\partial y},$$

$$\tau_{zz} = -2\tilde{\mu}\frac{\partial w}{\partial z} - \lambda\Big(\frac{\partial u}{\partial x} + \frac{\partial v}{\partial y} + \frac{\partial w}{\partial z}\Big), \qquad \tau_{yz} = \tau_{zy} = -\tilde{\mu}\Big(\frac{\partial v}{\partial z} + \frac{\partial w}{\partial y}\Big), \qquad q_z = -\tilde{k}\frac{\partial T}{\partial z}.$$

The equation set is closed by using the perfect gas law to relate temperature to pressure and density, the Sutherland viscosity formula for air[3] to determine viscosity as a function of temperature, the Stokes relation to give the bulk viscosity, and the assumption of constant Prandtl number to determine the conductivity of the gas. The two turbulent transport coefficients, μ_t and k_t, are determined using the Baldwin-Lomax turbulence model[4].

$$p = (\gamma - 1)\Big(e - \frac{1}{2}\rho(u^2 + v^2 + w^2)\Big),$$

$$\tilde{\mu} \equiv \mu + \mu_t, \qquad \frac{\mu}{\mu_r} = \frac{T_r + T_1}{T + T_1}\Big(\frac{T}{T_r}\Big)^{\frac{3}{2}},$$

$$\tilde{k} \equiv k + k_t, \qquad \lambda = -\frac{2}{3}\tilde{\mu},$$

$$Pr \equiv \frac{\gamma c_v \mu}{k}, \qquad Pr_t \equiv \frac{\gamma c_v \mu_t}{k_t},$$

where the subscript r represents a reference temperature and T_1 is taken to be 110°K. These equations were used for the present calculation in which temperatures where well below those where dissociation or ionization of the gas may take place.

The set of differential equations is fully described by imposing appropriate initial and boundary conditions. The initial conditions are not critical because the required solution is steady-state, therefore an arbitrary initial condition amounting to a rough

guess of the initial flow field and satisfying the constitutive relations can be imposed. The boundary conditions are determined by the physical nature of each boundary. At the surface of the body a no-slip condition is used with either an adiabatic wall or a fixed wall temperature. At the boundary outside of the bow shock wave, which is the free-stream, the flow conditions are fixed since they are uninfluenced by the interior flow field. In the streamwise direction the only relevant boundary is that at the end of the body; this is set by assuming that $\frac{\partial U}{\partial \xi} = 0$, which is physically consistent because the flow is either supersonic or within the boundary layer at this point. The boundaries in the meridional direction are set using bilateral symmetry considerations.

The Numerical Method

The numerical procedure used is a generalization to three dimensions of the implicit Gauss-Seidel line-relaxation technique developed by MacCormack for two dimensions and is derived from the volume formulation of the Navier-Stokes equations. The first-order difference equations are derived here, although the generalization to second-order spatial accuracy follows directly.

Consider a three-dimensional mesh made up of finite volumes with the flow variables stored at the centroids of each volume, and the corners of each volume stored as the x, y, z coordinates of the grid points. We can think of the discrete form of the volume formulation of the Navier-Stokes equations as a summation of the fluxes entering a finite volume:

$$\frac{\partial U}{\partial t} + \frac{1}{V} \sum_{V} \vec{F} \cdot \Delta \vec{S} = 0. \tag{2}$$

We now adopt a sign convention on $\vec{S}$ so that a component of $\vec{S}$ is positive when directed in increasing ξ, η, or ζ. We also break $\vec{F}$ into three parts as

$$\vec{F} = \vec{F}_+ + \vec{F}_- + \hat{\vec{F}},$$

where $\vec{F}_+$ represents the flux induced by the inviscid terms in the equations moving in the positive ξ, η, or ζ direction and $\vec{F}_-$ is the negatively moving flux. $\hat{\vec{F}}$ is the flux produced by the viscous stresses and thermal effects. Discretizing Equation (2) we have

$$\begin{aligned}
\left(U^{n+1}_{i,j,k} - U^{n}_{i,j,k}\right) + \frac{\Delta t}{V_{i,j,k}} \Big\{ & \left(\vec{F}^{n+1}_{+i,j,k} + \vec{F}^{n+1}_{-i+1,j,k} + \hat{\vec{F}}^{n+1}_{i,j,k}\right) \cdot \vec{S}_{i+\frac{1}{2}} - \left(\vec{F}^{n+1}_{+i-1,j,k} + \vec{F}^{n+1}_{-i,j,k} + \hat{\vec{F}}^{n+1}_{i-1,j,k}\right) \cdot \vec{S}_{i-\frac{1}{2}} \\
& + \left(\vec{F}^{n+1}_{+i,j,k} + \vec{F}^{n+1}_{-i,j+1,k} + \hat{\vec{F}}^{n+1}_{i,j,k}\right) \cdot \vec{S}_{j+\frac{1}{2}} - \left(\vec{F}^{n+1}_{+i,j-1,k} + \vec{F}^{n+1}_{-i,j,k} + \hat{\vec{F}}^{n+1}_{i,j-1,k}\right) \cdot \vec{S}_{j-\frac{1}{2}} \\
& + \left(\vec{F}^{n+1}_{+i,j,k} + \vec{F}^{n+1}_{-i,j,k+1} + \hat{\vec{F}}^{n+1}_{i,j,k}\right) \cdot \vec{S}_{k+\frac{1}{2}} - \left(\vec{F}^{n+1}_{+i,j,k-1} + \vec{F}^{n+1}_{-i,j,k} + \hat{\vec{F}}^{n+1}_{i,j,k-1}\right) \cdot \vec{S}_{k-\frac{1}{2}} \Big\} = 0,
\end{aligned} \tag{3}$$

where $\vec{S}_{i+\frac{1}{2}}$ denotes the surface vector of the surface between point i, j, k and point $i+1, j, k$, with the other surface vectors defined similarly. (Note that because of the definition of $\vec{S}$ the above summation is made up of positively and negatively signed components.) We let

$$F'_{+i,j,k} \equiv \frac{\vec{F}_{+i,j,k} \cdot \vec{S}_{i+\frac{1}{2}}}{\left|\vec{S}_{i+\frac{1}{2}}\right|}, \qquad G'_{+i,j,k} \equiv \frac{\vec{F}_{+i,j,k} \cdot \vec{S}_{j+\frac{1}{2}}}{\left|\vec{S}_{j+\frac{1}{2}}\right|}, \qquad H'_{+i,j,k} \equiv \frac{\vec{F}_{+i,j,k} \cdot \vec{S}_{k+\frac{1}{2}}}{\left|\vec{S}_{k+\frac{1}{2}}\right|},$$

with the other components of the fluxes defined similarly. Linearizing the flux vectors in time gives

$$F'^{n+1}_{+ijk} = F'^{n}_{+ijk} + A'^{n}_{+ijk}\delta U^{n}_{ijk} + O(\Delta t^2),$$
$$G'^{n+1}_{+ijk} = G'^{n}_{+ijk} + B'^{n}_{+ijk}\delta U^{n}_{ijk} + O(\Delta t^2),$$
$$H'^{n+1}_{+ijk} = H'^{n}_{+ijk} + C'^{n}_{+ijk}\delta U^{n}_{ijk} + O(\Delta t^2).$$

Where A', B', and C' are the Jacobians of the flux vectors of F', G', and H' with respect to U, and $\delta U^n \equiv U^{n+1} - U^n$. Here we are using first-order accuracy in time because we are interested in the steady-state solution and temporal accuracy is not required. The method may be made second-order accurate in time with some effort. The finite volume Navier-Stokes equations may now be written more succinctly using difference operators as

$$\begin{aligned}
&\left\{ I + \frac{\Delta t}{V_{ijk}} \left[\frac{D_-}{\Delta \xi} \cdot A'^{n}_{+ijk} \left|\vec{S}_{i+\frac{1}{2}}\right| + \frac{D_+}{\Delta \xi} \cdot A'^{n}_{-i-1jk} \left|\vec{S}_{i-\frac{1}{2}}\right| + \frac{D_-}{\Delta \eta} \cdot B'^{n}_{+ijk} \left|\vec{S}_{j+\frac{1}{2}}\right| \right.\right. \\
&\left.\left. + \frac{D_+}{\Delta \eta} \cdot B'^{n}_{-ij-1k} \left|\vec{S}_{j-\frac{1}{2}}\right| + \cdots + \frac{D}{\Delta \xi} \cdot \hat{F}'^{n+1}_{ijk} \left|\vec{S}_{i+\frac{1}{2}}\right| + \frac{D}{\Delta \eta} \cdot \hat{G}'^{n+1}_{ijk} \left|\vec{S}_{j+\frac{1}{2}}\right| + \cdots \right] \right\} \delta U^{n}_{ijk} \\
&\quad = -\frac{\Delta t}{V_{ijk}} \left[\frac{D_-}{\Delta \xi} \cdot F'^{n}_{+ijk} \left|\vec{S}_{i+\frac{1}{2}}\right| + \frac{D_+}{\Delta \xi} \cdot F'^{n}_{-i-1jk} \left|\vec{S}_{i-\frac{1}{2}}\right| \right. \\
&\quad \left. + \frac{D_-}{\Delta \eta} \cdot G'^{n}_{+ijk} \left|\vec{S}_{j+\frac{1}{2}}\right| + \frac{D_+}{\Delta \eta} \cdot G'^{n}_{-ij-1k} \left|\vec{S}_{j-\frac{1}{2}}\right| + \cdots \right],
\end{aligned} \tag{4}$$

We let

$$\hat{F}'^{n+1}_{ijk} = \hat{F}'^{n}_{ijk} + \delta \hat{F}'^{n}_{ijk},$$

with similar expressions for the other two viscous fluxes. We apply the thin-layer assumption to the derivatives of the implicit viscous terms. This implies that the differences with respect to η are much larger than those with respect to ξ or ς,

$$\frac{D}{\Delta \eta}\delta \hat{G}' \gg \frac{D}{\Delta \xi}\delta \hat{F}', \ \frac{D}{\Delta \varsigma}\delta \hat{H}' \simeq 0.$$

Thus we need only find an expression for $\delta \hat{G}'$.

We define

$$S'_{jx} = \frac{\vec{i}_x \cdot \vec{S}_{j+\frac{1}{2}}}{\left|\vec{S}_{j+\frac{1}{2}}\right|}, \quad S'_{jy} = \frac{\vec{i}_y \cdot \vec{S}_{j+\frac{1}{2}}}{\left|\vec{S}_{j+\frac{1}{2}}\right|}, \quad \text{and} \quad S'_{jz} = \frac{\vec{i}_z \cdot \vec{S}_{j+\frac{1}{2}}}{\left|\vec{S}_{j+\frac{1}{2}}\right|},$$

to obtain

$$\hat{G}' = \hat{F}S'_{jx} + \hat{G}S'_{jy} + \hat{H}S'_{jz}.$$

The rotated viscous flux $\hat{G}'$ is made up of stresses that contain derivatives with respect to the Cartesian variables x, y, z which must be changed to the general variables ξ, η, ς. However, if we apply the thin layer assumption, the derivatives with respect to ξ and ς may be neglected. Therefore we have

$$\frac{\partial}{\partial x} = \frac{\partial \eta}{\partial x}\frac{\partial}{\partial \eta}, \qquad \frac{\partial}{\partial y} = \frac{\partial \eta}{\partial y}\frac{\partial}{\partial \eta}, \qquad \frac{\partial}{\partial z} = \frac{\partial \eta}{\partial z}\frac{\partial}{\partial \eta}.$$

The derivatives of the mesh variables with respect to the Cartesian variables are determined using the relations derived from the coordinate transformation matrices

$$\frac{\partial \eta}{\partial x} = \frac{1}{V}\left(\frac{\partial y}{\partial \varsigma}\frac{\partial z}{\partial \xi} - \frac{\partial y}{\partial \xi}\frac{\partial z}{\partial \varsigma}\right) = \frac{1}{V}S'_{jx}\left|\vec{S}_{j+\frac{1}{2}}\right|,$$
$$\frac{\partial \eta}{\partial y} = \frac{1}{V}\left(\frac{\partial x}{\partial \xi}\frac{\partial z}{\partial \varsigma} - \frac{\partial x}{\partial \varsigma}\frac{\partial z}{\partial \xi}\right) = \frac{1}{V}S'_{jy}\left|\vec{S}_{j+\frac{1}{2}}\right|,$$
$$\frac{\partial \eta}{\partial z} = \frac{1}{V}\left(\frac{\partial x}{\partial \varsigma}\frac{\partial y}{\partial \xi} - \frac{\partial x}{\partial \xi}\frac{\partial y}{\partial \varsigma}\right) = \frac{1}{V}S'_{jz}\left|\vec{S}_{j+\frac{1}{2}}\right|.$$

Finally, using these changes of variable, we can rewrite $\delta\hat{G}'$ as

$$\delta\hat{G}' = -\frac{\left|\vec{S}_{j+\frac{1}{2}}\right|}{V} M_\eta \frac{\partial}{\partial \eta}(\delta \mathbf{V}), \tag{5}$$

where

$$M_\eta = \begin{pmatrix} 0 & 0 & 0 & 0 & 0 \\ 0 & S_{jx}^2(2\tilde{\mu}+\lambda)+\tilde{\mu}(S_{jy}^2+S_{jz}^2) & S_{jx}S_{jy}(\tilde{\mu}+\lambda) & S_{jx}S_{jz}(\tilde{\mu}+\lambda) & 0 \\ 0 & S_{jx}S_{jy}(\tilde{\mu}+\lambda) & S_{jy}^2(2\tilde{\mu}+\lambda)+\tilde{\mu}(S_{jx}^2+S_{jz}^2) & S_{jy}S_{jz}(\tilde{\mu}+\lambda) & 0 \\ 0 & S_{jx}S_{jz}(\tilde{\mu}+\lambda) & S_{jy}S_{jz}(\tilde{\mu}+\lambda) & S_{jz}^2(2\tilde{\mu}+\lambda)+\tilde{\mu}(S_{jx}^2+S_{jy}^2) & 0 \\ 0 & m_{5,2} & m_{5,3} & m_{5,4} & m_{5,5} \end{pmatrix}$$

$$m_{5,2} = \tilde{u}\left(S_{jx}^2(2\tilde{\mu}+\lambda)+\tilde{\mu}(S_{jy}^2+S_{jz}^2)\right) + \tilde{v}S_{jx}S_{jy}(\tilde{\mu}+\lambda) + \tilde{w}S_{jx}S_{jz}(\tilde{\mu}+\lambda),$$
$$m_{5,3} = \tilde{u}S_{jx}S_{jy}(\tilde{\mu}+\lambda) + \tilde{v}\left(S_{jy}^2(2\tilde{\mu}+\lambda)+\tilde{\mu}(S_{jx}^2+S_{jz}^2)\right) + \tilde{w}S_{jy}S_{jz}(\tilde{\mu}+\lambda),$$
$$m_{5,4} = \tilde{u}S_{jx}S_{jz}(\tilde{\mu}+\lambda) + \tilde{v}S_{jy}S_{jz}(\tilde{\mu}+\lambda) + \tilde{w}\left(S_{jz}^2(2\tilde{\mu}+\lambda)+\tilde{\mu}(S_{jx}^2+S_{jy}^2)\right),$$
$$m_{5,5} = \frac{\tilde{k}}{c_v}(S_{jx}^2+S_{jy}^2+S_{jz}^2).$$

$$\delta\mathbf{V} = \begin{pmatrix} \delta\rho \\ \delta u \\ \delta v \\ \delta w \\ \delta e_t \end{pmatrix},$$

Here the bars on the velocities represent the average value of that velocity between the two volumes in question. We can change variables from $\delta\mathbf{V}$ to δU by defining the Jacobian N to be $N = \frac{\partial \mathbf{V}}{\partial U}$, so that $\delta\mathbf{V} = N\delta U$. Thus we finally have

$$\frac{D_-}{\Delta\eta}\delta\hat{G}^n_{i,j,k}\left|\vec{S}_{j+\frac{1}{2}}\right| = -\frac{D_-}{\Delta\eta}\cdot\frac{\left|\vec{S}_{j+\frac{1}{2}}\right|^2}{V_{i,j,k}} M_\eta\left(\frac{D_+}{\Delta\eta}\cdot N\delta U_{i,j,k}\right). \tag{6}$$

Combining Equations (4) and (6), we have the final form of the finite volume difference equation which approximates the Navier-Stokes equations. The equation is given below

with the quantities that are known at time n on the right hand side, and those that must be solved implicitly at time $n+1$ on the left.

$$\left\{ I + \frac{\Delta t}{V_{ijk}} \left[\frac{D_-}{\Delta \xi} A'^{n}_{+ijk} \left| \vec{S}_{i+\frac{1}{2}} \right| + \frac{D_+}{\Delta \xi} A'^{n}_{+i-1jk} \left| \vec{S}_{i-\frac{1}{2}} \right| + \frac{D_-}{\Delta \eta} B'^{n}_{+ijk} \left| \vec{S}_{j+\frac{1}{2}} \right| + \frac{D_+}{\Delta \eta} B'^{n}_{+ij-1k} \left| \vec{S}_{j-\frac{1}{2}} \right| \right.\right.$$

$$\left.\left. + \frac{D_-}{\Delta \eta} C'^{n}_{+ijk} \left| \vec{S}_{k+\frac{1}{2}} \right| + \frac{D_+}{\Delta \eta} C'^{n}_{+ijk-1} \left| \vec{S}_{k-\frac{1}{2}} \right| - \frac{D_-}{\Delta \eta} \cdot \frac{\left| \vec{S}_{j+\frac{1}{2}} \right|^2}{V_{ijk}} M_\eta \left(\frac{D_+}{\Delta \eta} \cdot N \right) \right] \right\} \delta U^n_{ijk}$$

$$= -\frac{\Delta t}{V_{ijk}} \left[\frac{D_-}{\Delta \xi} F'^{n}_{+ijk} \left| \vec{S}_{i+\frac{1}{2}} \right| + \frac{D_+}{\Delta \xi} F'^{n}_{+i-1jk} \left| \vec{S}_{i-\frac{1}{2}} \right| + \cdots \right] \equiv \Delta U^n_{ijk}. \tag{7}$$

This completes the derivation of the difference equation used to solve the Navier-Stokes equations.

The implementation of the boundary conditions for the explicit side of the difference equation is straightforward. ΔU^n is computed using the prescribed boundary conditions mentioned above. However, the implicit boundary conditions are more complicated. Let us write Equation (7) in terms of 5×5 block matrices

$$\tilde{A} \delta U^n_{ijk} + \tilde{B} \delta U^n_{ij+1k} + \tilde{C} \delta U^n_{ij-1k} + \tilde{D} \delta U^n_{i+1jk} + \tilde{E} \delta U^n_{i-1jk} + \tilde{F} \delta U^n_{ijk+1} + \tilde{G} \delta U^n_{ijk-1} = \Delta U^n_{ijk}, \tag{8}$$

where the matrices with tildes are defined implicitly from Equation (7). We may write Equation (8) in matrix form at a general i and k location as

$$\begin{pmatrix} I & -E_J & & & & & & \\ \tilde{B}_{J-1} & \tilde{A}_{J-1} & \tilde{C}_{J-1} & & & & & \\ & \ddots & & & & & & \\ & & \tilde{B}_j & \tilde{A}_j & \tilde{C}_j & & & \\ & & & \ddots & & & & \\ & & & & \tilde{B}_2 & \tilde{A}_2 & \tilde{C}_2 & \\ & & & & & -E_1 & I & \end{pmatrix} \cdot \begin{pmatrix} \delta U_{ijk} \\ \delta U_{ij-1k} \\ \vdots \\ \delta U_{ijk} \\ \vdots \\ \delta U_{i2k} \\ \delta U_{i1k} \end{pmatrix} = \begin{pmatrix} 0 \\ \Delta U_{ij-1k} + \cdots \\ \vdots \\ \Delta U_{ijk} + \cdots \\ \vdots \\ \Delta U_{i2k} + \cdots \\ 0 \end{pmatrix}. \tag{9}$$

The top and bottom equations are used to set the freestream and the wall boundaries respectively. The freestream boundary is easy to set because it is a supersonic inflow so that the flow field remains invariant. Thus we have $\delta U_{ijk} = 0$, which implies that $E_J = 0$, and therefore $\tilde{B}_{J-1}$ is redundant. For the wall boundary condition, we impose that there is no-slip at the wall, the normal derivative of pressure at the wall is zero (from boundary layer theory), and that a wall temperature condition holds depending on whether the wall has a fixed temperature or is adiabatic. These conditions at the wall fix the flow field at the wall uniquely and imply that $\delta u'_1 = -\delta u'_2$, $\delta v'_1 = -\delta v'_2$, $\delta w'_1 = -\delta w'_2$, and $\delta p_1 = \delta p_2$. For the internal energy, we impose

$$\delta ei_1 = \begin{cases} \delta ei_2 & \text{adiabatic wall;} \\ 2\delta ei_{\text{wall}} - \delta ei_2 & \text{fixed wall temperature.} \end{cases}$$

Here we are using a grid where a dummy point within the body is used (subscript $j = 1$) to set the boundary at the body surface. The primes on the velocities represent rotated velocities given by

$$u' = uS_{ix} + vS_{iy} + wSiz,$$

$$v' = uS_{jx} + vS_{jy} + wSjz,$$

$$w' = uS_{kx} + vS_{ky} + wSkz.$$

We can write the wall boundary condition in matrix form as $\mathbf{T}_1\delta U_1 = \mathbf{T}_2\delta U_2$ which implies that $E_1 = \mathbf{T}_1^{-1}\mathbf{T}_2$. Therefore the next to last equation in (9) may be written as

$$\tilde{B}_2\delta U_{i3k} + \left(\tilde{A}_2 + \tilde{C}_2E_1\right)\delta U_{i2k} = \Delta U_{i2k}.$$

We define

$$\tilde{A}'_2 \equiv \left(\tilde{A}_2 + \tilde{C}_2E_1\right).$$

Then by contracting the upper and lower equations, we rewrite (9) as

$$\begin{pmatrix} \tilde{A}_{J-1} & \tilde{C}_{J-1} & & & \\ & \ddots & & & \\ & \tilde{B}_j & \tilde{A}_j & \tilde{C}_j & \\ & & & \ddots & \\ & & & \tilde{B}_2 & \tilde{A}'_2 \end{pmatrix} \begin{pmatrix} \delta U_{iJ-1k} \\ \vdots \\ \delta U_{ijk} \\ \vdots \\ \delta U_{i2k} \end{pmatrix} = \begin{pmatrix} \Delta U_{iJ-1k} + \cdots \\ \vdots \\ \Delta U_{ijk} + \cdots \\ \vdots \\ \Delta U_{i2k} + \cdots \end{pmatrix}. \tag{10}$$

A similar treatment of the boundaries in the i and k directions for the implicit side of the Equation (7) is required. The procedure generalizes from the above discussion directly.

This completes the derivation of the technique to solve the Navier-Stokes equations using Gauss-Seidel line-relaxation. The procedure to solve these difference equations is as follows:

1. Solve ΔU^n_{ijk}, the right hand side of Equation (7), for the whole flow field using data at the current time level n.
2. Use ΔU^n_{ijk} as a driving term to solve the left hand side of the equation, using the latest available data (*i.e.* using a Gauss-Seidel technique). This is done by solving a block tridiagonal matrix equation in δU^n_{ijk} along a particular j line in the flow field. The solution line is swept through the flow field from the farthest downstream i plane to the upstream i plane, then the reverse is performed. The j solution line is swept through all k locations during each streamwise pass. Thus, with a large enough time step, each point in the flow field could conceivably be influenced by every other point.
3. Update the solution using $U^{n+1}_{ijk} = U^n_{ijk} + \delta U^n_{ijk}$, and continue the process until convergence is achieved.

Implementing second-order spatial differencing is fairly straightforward and is accomplished by replacing for example $F_{+i+\frac{1}{2}} = F_{+i}$ (first-order), with $F_{+i+\frac{1}{2}} = \frac{3}{2}F_{+i} - \frac{1}{2}F_{+i-1}$

(second-order). In the j direction on the implicit side, the data from the most recent time step is used to compute the fluxes originating from two cells away from the cell in question. This maintains the block tridiagonal structure of the matrix solution without sacrificing second-order accuracy. Although the fluxes from two cells away are somewhat lagged in time, this becomes unimportant as the solution converges to a steady-state.

The Shock Fitting Routine

The technique of shock-fitting was originally developed by Moretti[5], however the method used for this solution is somewhat different and, as a result, is presented here. The bow shock wave that envelops a hypersonic body is represented as a surface of discontinuity which is moved through the flow field in a physically consistent manner. Computationally, the shock wave is located at a constant j mesh surface and acts as a boundary in the solution. The initial position of the shock wave is guessed at the beginning of the calculation, and then the shock wave is moved through the mesh after each time step until the steady-state position is reached. The procedure for each iteration is to solve the discretized Navier-Stokes equations for the entire flow field. Then the shock wave velocity is computed at the mesh surface that represents the shock wave. The mesh is then reconfigured by moving the shock wave surface inward or outward, and all of the other interior grid points are adjusted in a consistent manner.

The shock wave velocity at each point is found by solving two of the Rankine-Hugoniot shock jump relations for an oblique shock wave and one characteristic relation for a backward-moving characteristic. We denote freestream conditions with a subscript 0, the conditions at a location immediately behind the shock with a subscript SHK, and the conditions at the centroid of the first volume behind the shock surface with a subscript 1. This nomenclature is used because the shock surface is located between the centroids of two finite volumes, *i.e.* there is a finite distance between the shock surface and the first downstream point where data exists. The characteristic relation is used to tie the conditions at these two locations together. The magnitude of the shock wave velocity is denoted as w_{SHK} and has direction parallel to the freestream velocity.

The relevant shock jump equations[3] for a shock moving with speed w_{SHK} are

$$M_{n0} = \frac{u_{n0} - w_{SHK}}{c_0} = \sqrt{\frac{1}{2\gamma}\left[(\gamma+1)\frac{p_{SHK}}{p_0} + (\gamma-1)\right]}$$

and

$$\frac{u_{nSHK} - w_{SHK}}{u_{n0} - w_{SHK}} = \frac{(\gamma-1)M_{n0}^2 + 2}{(\gamma+1)M_{n0}^2}.$$

The relation for a backward running characteristic is

$$u_{nSHK} - u_{n1} = \frac{1}{\rho c}(p_{SHK} - p_1).$$

We can solve implicitly for $\frac{p_{SHK}}{p_0}$ as

$$\frac{p_{SHK}}{p_0} - \frac{\rho c}{p_0}\left(u_{n0} - u_{n1} - \frac{c_0\left(\frac{p_{SHK}}{p_0} - 1\right)}{\sqrt{\frac{\gamma}{2}\left[(\gamma+1)\frac{p_{SHK}}{p_0} + (\gamma-1)\right]}}\right) - \frac{p_1}{p_0} = 0, \tag{11}$$

and for the shock speed as

$$w_{SHK} = u_{n0} - c_0\sqrt{\frac{\gamma}{2}\left[(\gamma+1)\frac{p_{SHK}}{p_0} + (\gamma-1)\right]}. \tag{12}$$

The element of the shock surface under consideration is moved a distance $w_{SHK}\Delta t$ in the direction parallel to $\bar{u}_0$. The point where the plane formed by the new shock surface intersects the surrounding mesh lines is found, the interior of the mesh is adjusted, and the change in volume of each volume is saved to account for the unsteady mesh transformation terms in the calculation of the surface fluxes.

It should be noted that the shock-fitting technique has the advantage of satisfying the Rankine-Hugoniot shock relations exactly at a single surface in the computation, rather than smearing the shock wave across several grid surfaces as in a shock capturing method. Thus fewer mesh surfaces are needed in the vicinity of the bow shock wave. Any imbedded shock waves in the flow field such as the canopy and strake induced shocks are captured by the numerical method.

Results of Test Cases

Biconic Results

The numerical method was tested on two different configurations. The first was a spherically capped biconic body travelling through air at a Mach number of 7.97 with a characteristic Reynolds number of 1.2×10^8/m. This configuration is of interest because it has been studied numerically and experimentally[2,6,7,8]. It consists of a spherical cap of radius r_n joined to a cone of half angle 10.5°, which joins a second cone of half angle of 7.0° at a point 21.5 nose radii from the tip. Bilateral symmetry was assumed and a body-fitted mesh was generated algebraically using exponential stretching away from the body surface and along the cone. The initial bow shock wave location was guessed to be a paraboloid of revolution, and then the shock was allowed to move during the solution as described above. A cross-section of the initial mesh through the bilateral plane of symmetry is shown in Figure 1.

The solution was performed in two sections, first a converged result for the nose section (about $4r_n$ long) was obtained. Then this solution was used as an inflow boundary for the afterbody section of the calculation. This is physically correct because the flow is purely supersonic or within the boundary layer at the plane where the solution was broken. This solution technique is more efficient than performing the entire calculation at once because the flow field around the afterbody is dependent on that around the nose section. Therefore, until the solution for the nose is converged, the afterbody solution will not progress to the correct solution and cannot converge. The

converged solution was obtained in 120 iterations for the nose section on a mesh with 30 points in the streamwise direction, 20 in the direction normal to the body, and 18 in the meridional direction. The results for the afterbody were computed in 180 iterations on a 18×20×18 mesh. A maximum CFL number of 1500 was used. The converged grid shape is shown in Figure 2 with the shock wave position indicated. Clearly the grid has been deformed greatly and has moved a significant physical distance. A plot of the surface pressure distribution on the afterbody compared to experimental evidence from Coutler and Carver[8] is given in Figure 3. The results show good agreement with experiment, with a maximum deviation of about 3%. A plot showing velocity profiles at two x/r_n locations is presented as Figure 4; it shows the well defined boundary layer which has been resolved by the method (the y^+ at the first point from the wall ranged from 0.3 to 1.2 in this case). Figure 5 is a plot of the temperature profile at the same two x/r_n locations. It should be noted that the solution is for a fixed wall temperature of 311.1 °K. The figure shows a very good resolution of the very large temperature gradient near the wall and the inflection point in the temperature distribution caused by the interaction of the cooled wall with the high temperature near-wall stream. The shock standoff distance computed with the current method agrees with the results of Scherr and Shang[7] to three significant figures.

A second solution of the zero angle of attack cone was performed with the same number of points in the grid, but with a near-wall spacing 3.0 times finer than the previous result (the y^+ for the first point from the wall was reduced by a factor of 2.9). The boundary layer and thermal layer are essentially identical for each case. The number of time steps required to reach a steady-state remained the same.

The flow field over the same body at a 7.0° angle of attack with the same flow conditions was also computed. The solution was obtained in 135 iterations for the nose section and 200 iterations for the afterbody. This is about a 10% increase over the zero angle of attack case. The final grid is given in Figure 6 and shows that the bow shock wave is swept more closely to the body on the windward side than on the leeward side. The asymmetry is also evident in the surface pressure plot for the windward and leeward sides of the body, which is given in Figure 7.

X24C Hypersonic Vehicle Results

The flow field over the X24C-10D hypersonic vehicle was computed for free-stream conditions of $M_\infty = 5.95$, an angle of attack of 6.0°, and a characteristic Reynolds number of 16.4×10^6/m. The X24C was a proposed configuration for a second generation space shuttle which has a spherically blunted nose, a canopy, and wings and strakes in the aft section of the aircraft. This body is a difficult test case for the numerical method with several complicated physical phenomena occurring in the flow field. The grid used was provided by Shang and Scherr[1] and is comprised of $60 \times 18 \times 28$ points for the nose and midsection of the body, and $58 \times 18 \times 55$ points for the afterbody, or a total of 87,660 grid points. The surface geometry of the X24C is presented in Figure 8. In this case the solution was broken into four sections to improve the efficiency of the solution and also to allow each section to fit in core memory (*i.e.* less than two million

words available on a Cray X-MP 48).

The results show good agreement with the results of Shang and Scherr[1] and the experimental results[9,10,11]. The numerical method accurately predicts the surface pressure on the vehicle except in the tail region on the leeward side, as seen in Figure 9. The poor resolution of the tail surface pressure is probably caused by the coarse grid near the tail which is shown in Figure 10. Shang and Scherr used twice as many grid points in the meridional direction and were able to predict the pressure more accurately, but a finer grid could not be used in this study because of the memory limitation. Figure 10 also demonstrates that the numerical technique does not require many mesh points in the flow field where the gradients are relatively small. Also the shock-fitting method will resolve the strong bow shock wave with a coarse mesh in the vicinity of the shock wave. This results in an efficient use of grid points in the normal direction. Figure 11 shows the Mach number distribution on the plane of symmetry, including the shock wave and recompression of the flow caused by the canopy.

The next five figures are for data at the $x/r_n = 108$ plane where much of the experimental data was taken[9,10,11]. The first plot is a pitot pressure survey with experimental points[10] indicating the location of the enveloping shock wave. The agreement with experiment is very good, and the results also compare well with those of Shang and Scherr[1]. Figure 14 is a plot of the grid at $x/r_n = 108$, which shows the location of the fitted bow shock surface in relation to the experimental results[10]. The agreement is very good, indicating that the shock-fitting routine produces an accurate shock location even where the shock is oblique. Figure 14 shows the surface pressure distribution versus the normalized arc length, $\varsigma/\varsigma_{MAX}$, at this x/r_n location. ($\varsigma/\varsigma_{MAX} = 0$ is the leeward point and $\varsigma/\varsigma_{MAX} = 1$ is the windward point.) The numerical results agree very well with experiment[9]. The peak in pressure at $\varsigma/\varsigma_{MAX} = 0.58$ is caused by the protrusion of the leading edge of the body into the flow. The sudden pressure drop to the lee of this point is a result of the expansion of the flow as it accelerates past the leading edge. Figure 15 is a plot of $\log St$ (a non-dimensional measure of the heat transfer) which shows at present a less accurate prediction of experimental results. The heat transfer is resolved well on the windward surface, but the results show poor agreement on the leeward surface. Figure 16 is a streamline trace on the leeward surface of the body. It shows that there is a large cross-flow separation bubble on the leeward surface at this x/r_n location. It is likely that the grid spacing, though able to resolve this structure in the flow and the surface pressure distribution, is inadequate to capture the temperature gradients in this region. The large dip in the Stanton number that occurs at $\varsigma/\varsigma_{MAX} = 0.06$ is located at the reattachment point of the vortical structure on the leeward surface. The heat transfer at this point is very small as would be expected due to the reduction in the velocity near the surface.

Figures 17 and 18 are streamline traces on the leeward surface of the body at the constant $x/r_n = 127.5$ plane where the central fin and the strake may be seen. The vortical structure that was present at $x/r_n = 108$ has become more pronounced and the separation region covers a larger portion of the body. A secondary vortex is evident

between the main vortex and the wall. Figure 19 is an enlargement of this structure and shows the level of complexity of the flow field that has been resolved. Figure 18 is a streamline trace at $x/r_n = 140$ where the fin and strake are at their maximum size. The vortical structure may be seen, but its strength has diminished because the strake has reduced the cross-flow which drives the vortex.

The number of iterations required to reach a steady-state solution varied as presented in the table below.

i Range	Iterations
1 - 24	190
24 - 60	190
60 - 84	120
84 - 118	250

Table 1. Iteration count for each solution section.

Qualitative Comments on the Results

The numerical method presented here has been shown to be a very efficient and competitive technique for the solution of the 3-D Navier-Stokes equations over hypersonic bodies. The iteration count for the solution of steady-state problems is on the order of one hundred for the test cases studied here. Further work needs to be done to vectorize the code and thus reduce the CPU time per iteration per grid point from the present 9.8×10^{-4}sec on a Cray X-MP 48.

The test cases have demonstrated several important features of the implicit Gauss-Seidel line-relaxation technique. The iteration count is about the same for each section of the X24C test case as for the biconic. An increase in the number of points in the meridional (ζ) direction does not increase the number of iterations required for a steady-state solution. The mesh spacing near the wall may be reduced without increasing the number of iterations or the CPU time needed for convergence.

The number of iterations required is proportional to the physical length of the section, the number of grid points in the i (streamwise) direction, the obliqueness of the shock wave, and the quality of the guess of the initial bow shock wave position. The convergence to steady-state is somewhat hindered by the coupling of the numerical method to the present shock-fitting technique. The steady-state solution is dependent on having the correct bow shock position and a converged flow field, thus both aspects of the solution must progress in time at approximately the same rate for an optimal convergence rate to be achieved. It appears from the nature of the solution development that the shock-fitting routine lags the solution of the flow field, slows down the total convergence rate, and increases the number of iterations required for a steady-state solution. In particular, the number of iterations to reach a steady-state for the biconic at $\alpha = 0.0°$ was reduced by a factor of two by specifying the converged grid location as the initial guess of the grid shape. This suggests the need for an improved shock-fitting technique or a different approach to capturing the bow shock wave to achieve the best convergence rate for this numerical method. However, in spite of this

inefficiency, the two procedures work well together and demonstrate a small iteration count for a steady-state solution.

Conclusions

In conclusion, a numerical method to solve the three-dimensional Navier-Stokes Equations for hypersonic bodies has been developed and tested. The test cases demonstrate that the method is robust and gives good results for a difficult problem. The technique has been shown to demonstrate a reduction in the number of time steps required to achieve a steady-state solution of approximately two orders of magnitude over an explicit method. The primary advantage of this method is that there is no penalty for making the mesh finer near the wall to resolve viscous and thermal effects. This algorithm represents a step toward being able to compute three-dimensional flow fields in a small number of iterations and with much less computer time.

References

1. Shang, J. S. and S. J. Scherr,"Navier-Stokes Solution of the Flow Field Around a Complete Aircraft," *AIAA Paper No. 85-1509*, 1985.
2. MacCormack, R. W., "Current Status of Numerical Solutions of the Navier-Stokes Equations," *AIAA Paper No. 85-0032*, 1985.
3. Anon., "Equations, Tables, and Charts for Compressible Flow," *NACA TR-1135.*
4. Baldwin, B. S. and H. Lomax, "Thin Layer Approximation and Algebraic Model for Separated Turbulent Flows," *AIAA Paper No. 78-257*, 1978.
5. Moretti, G., "Three-Dimensional, Supersonic, Steady Flows with any Number of Imbedded Shocks," *AIAA Paper No. 74-10*, 1974.
6. Shang, J. S. and R. W. MacCormack, "Flow Over a Biconic Configuration with an Afterbody Compression Flap – A Comparative Numerical Study," *AIAA Paper No. 83-1668*, 1983.
7. Scherr, S. J. and J. S. Shang, "Flows over Blunt Bodies Using a Flux-Splitting and Shock-Fitting Scheme," *AIAA Paper No. 86-0340*,1986.
8. Coutler, S. M. and D. B. Carver, "Heat Transfer Surface Pressure and Flow Field Surveys on the AEDC Biconic with Slices and Flaps at Mach 8-MAT Phase J," *AEDC-TR-81-V24*, July 1981.
9. Wannernwetsch, G. D., "Pressure Tests of the AFFDL X-24C-10D Model at Mach Numbers of 1.5, 3.0, 5.0, and 6.0," AEDC-DR-76-92, Von Karman Gas Dynamics Facility, Arnold Engineering Development Center, TN, November 1976.
10. Carver, D. B., "AFFDL X24C Flowfield Survey," Von Karman Gas Dynamics Facility, Arnold Engineering Development Center, TN, Project No. V41B-47, June, 1979.
11. Neumann, R. D., J. L. Patterson, and N. J. Sliski, "Aerodynamic Heating to the Hypersonic Research Aircraft X24C," *AIAA Paper No. 78-37*, 1978.
12. Kaul, U. K. and D. S. Chaussee, "A Comparative Study of the Parabolized Navier-Stokes Code Using Various Grid-Generation Techniques," *AIAA Paper No. 82-184*, 1982.

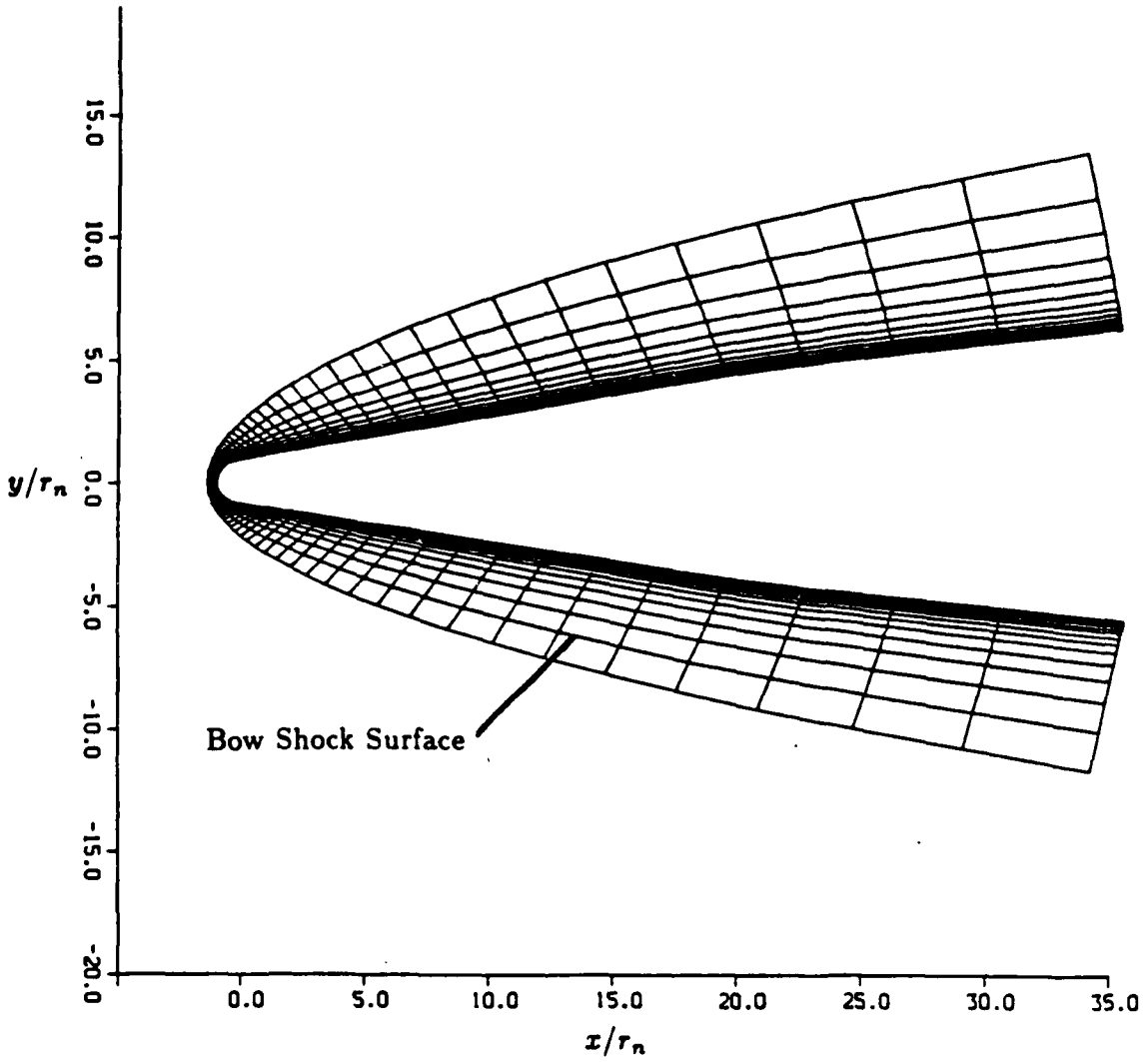

Figure 1. Initial Grid for Biconic Test Case. Grid is $45 \times 20 \times 18$. $M_\infty = 7.97$, $Re = 1.2 \times 10^8/\text{m}$

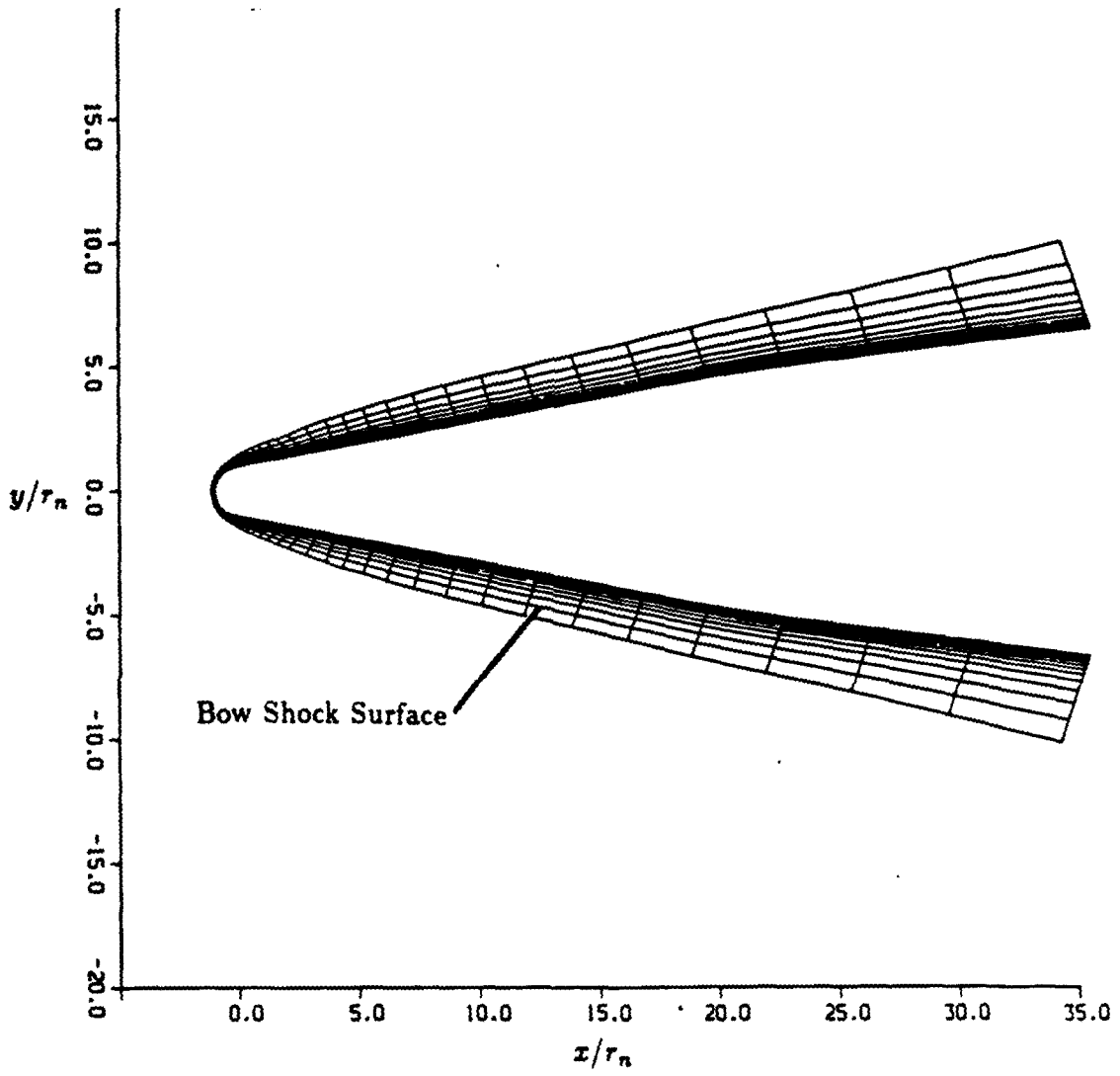

Figure 2. Converged Grid for Biconic Test Case.
$\alpha = 0.0°$, $M_\infty = 7.97$, $Re = 1.2 \times 10^8$/m.

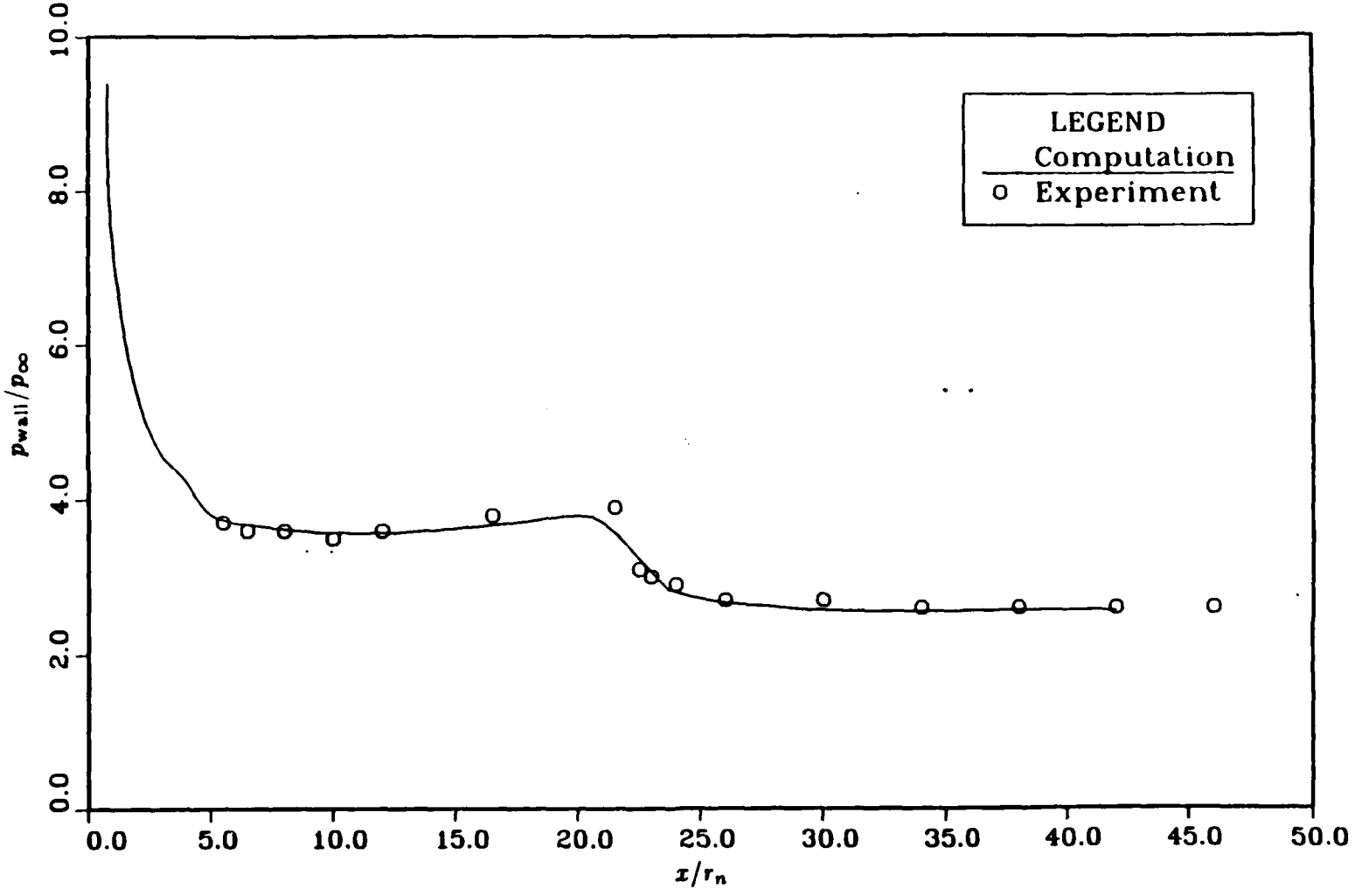

Figure 3. Comparison of Surface Pressure Distribution on Biconic. Experimental results are from Coutler and Carver[8]. $\alpha = 0.0°$, $M_\infty = 7.97$, $Re = 1.2 \times 10^8/\text{m}$.

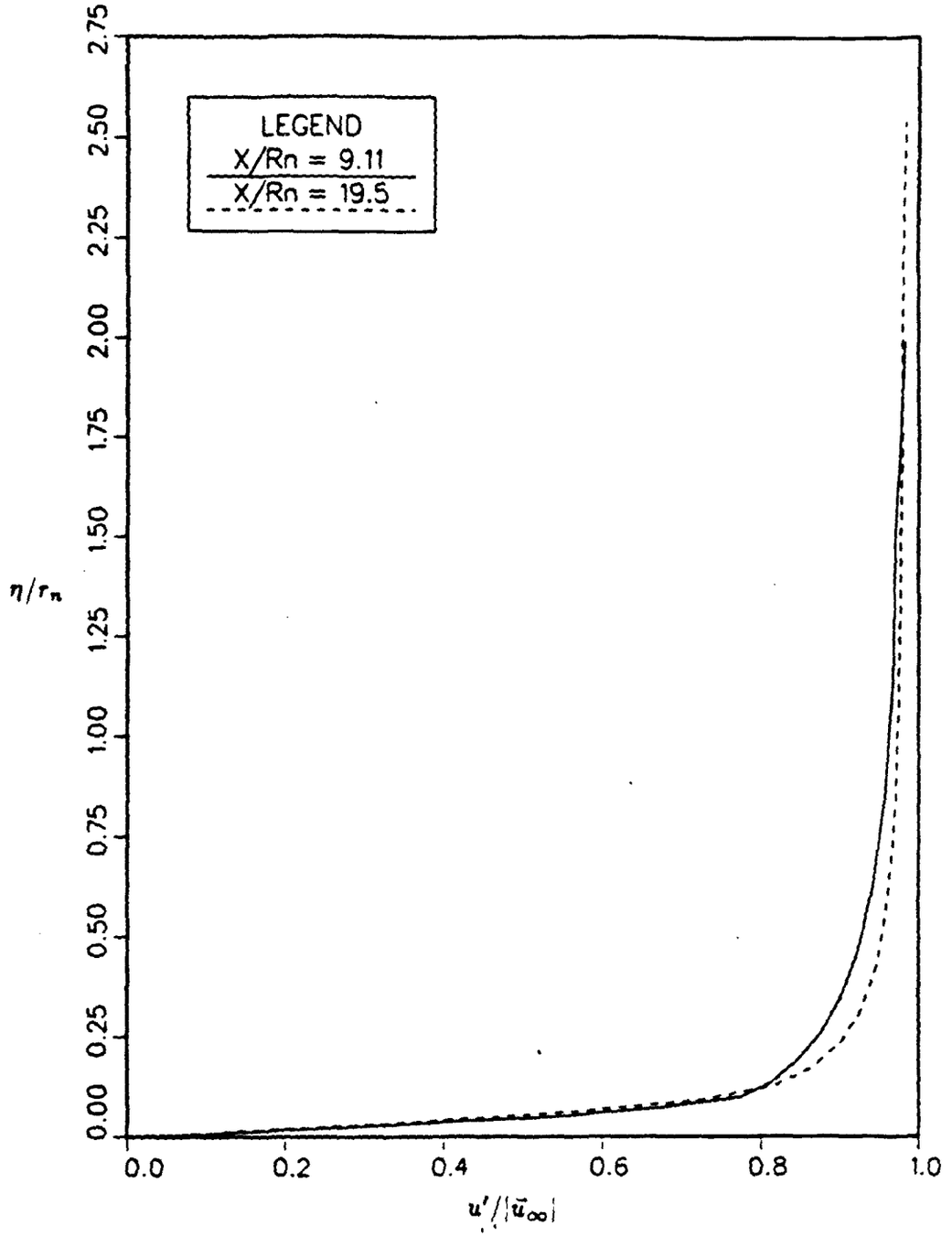

Figure 4. Velocity Profiles on Biconic Afterbody.
$\alpha = 0.0°$, $M_\infty = 7.97$, $Re = 1.2 \times 10^8$/m.

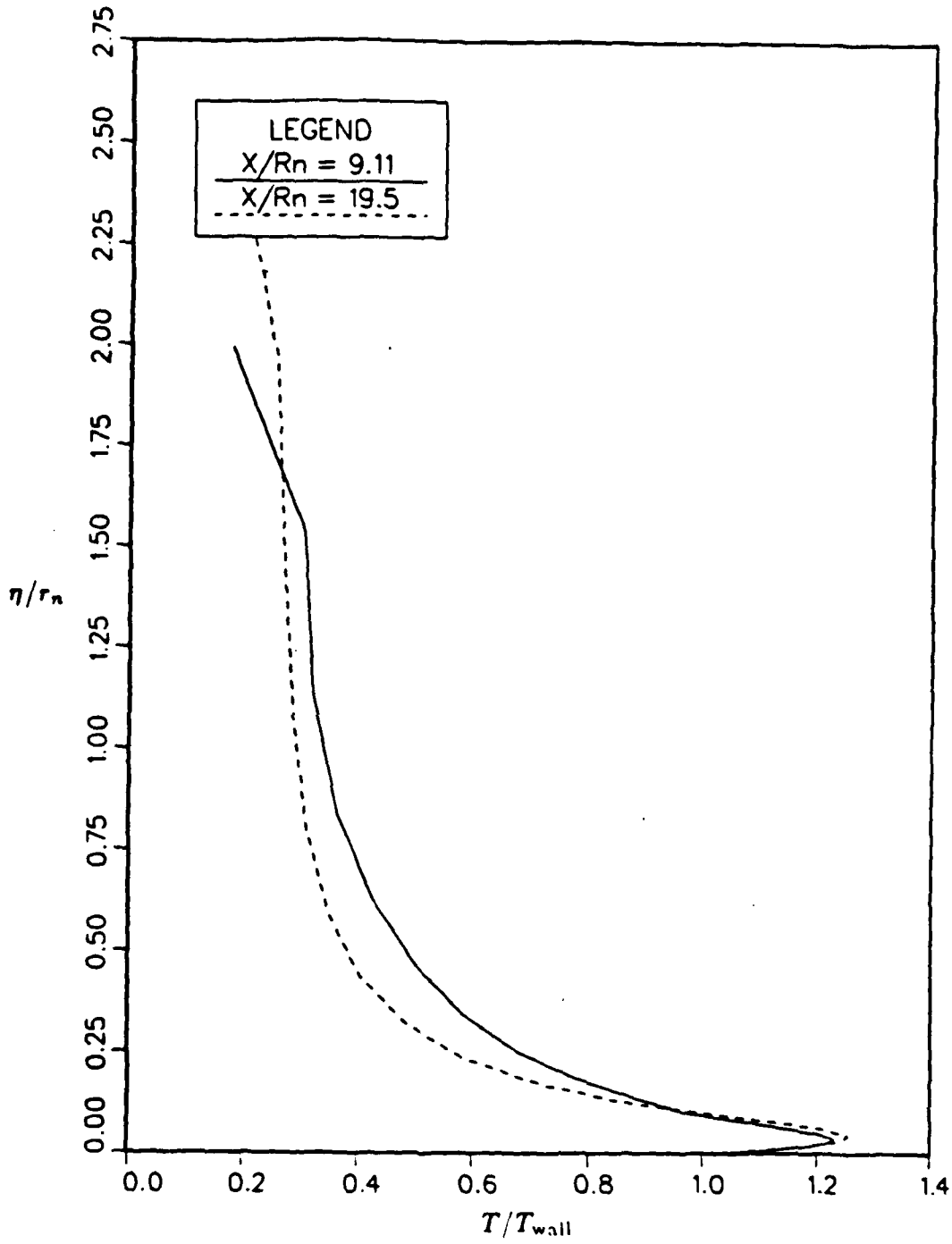

Figure 5. Temperature Profiles on Biconic Afterbody.
$\alpha = 0.0°$, $M_\infty = 7.97$, $Re = 1.2 \times 10^8/\text{m}$.

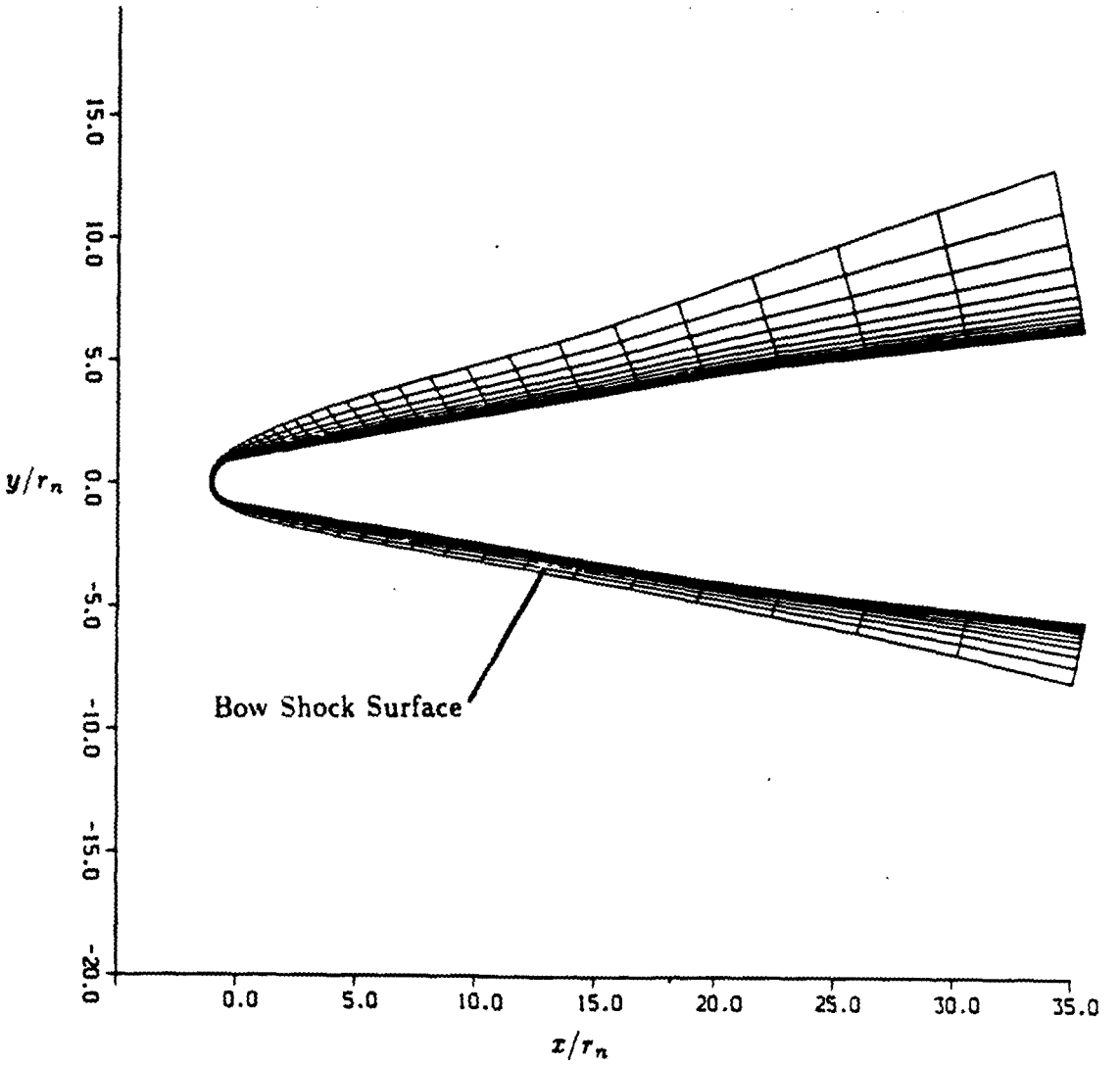

Figure 6. Converged Grid for Biconic Test Case.
$\alpha = 7.0°$, $M_\infty = 7.97$, $Re = 1.2 \times 10^8/\text{m}$.

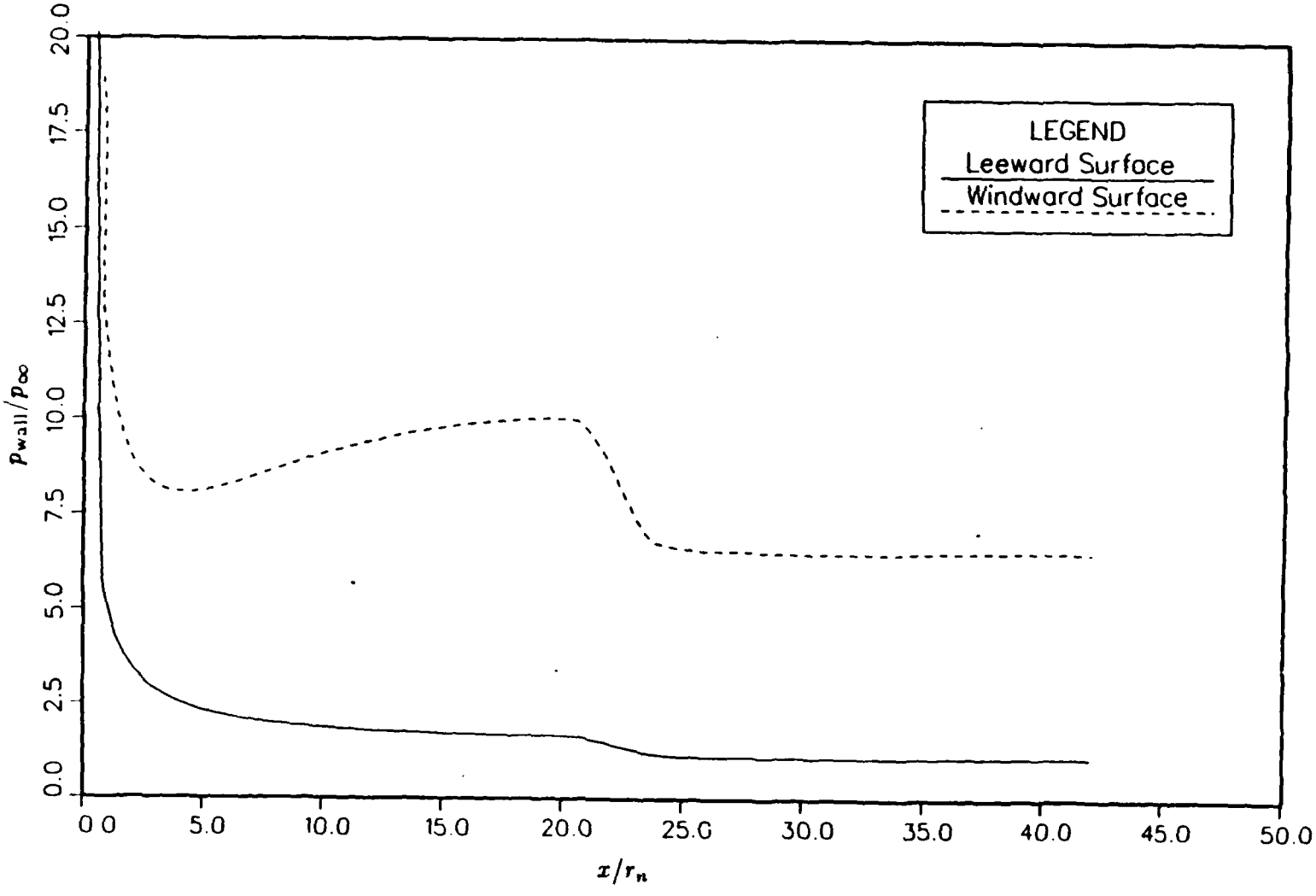

Figure 7. Surface Pressure Distribution on Biconic Afterbody.
$\alpha = 7.0°$, $M_\infty = 7.97$, $Re = 1.2 \times 10^6$/m.

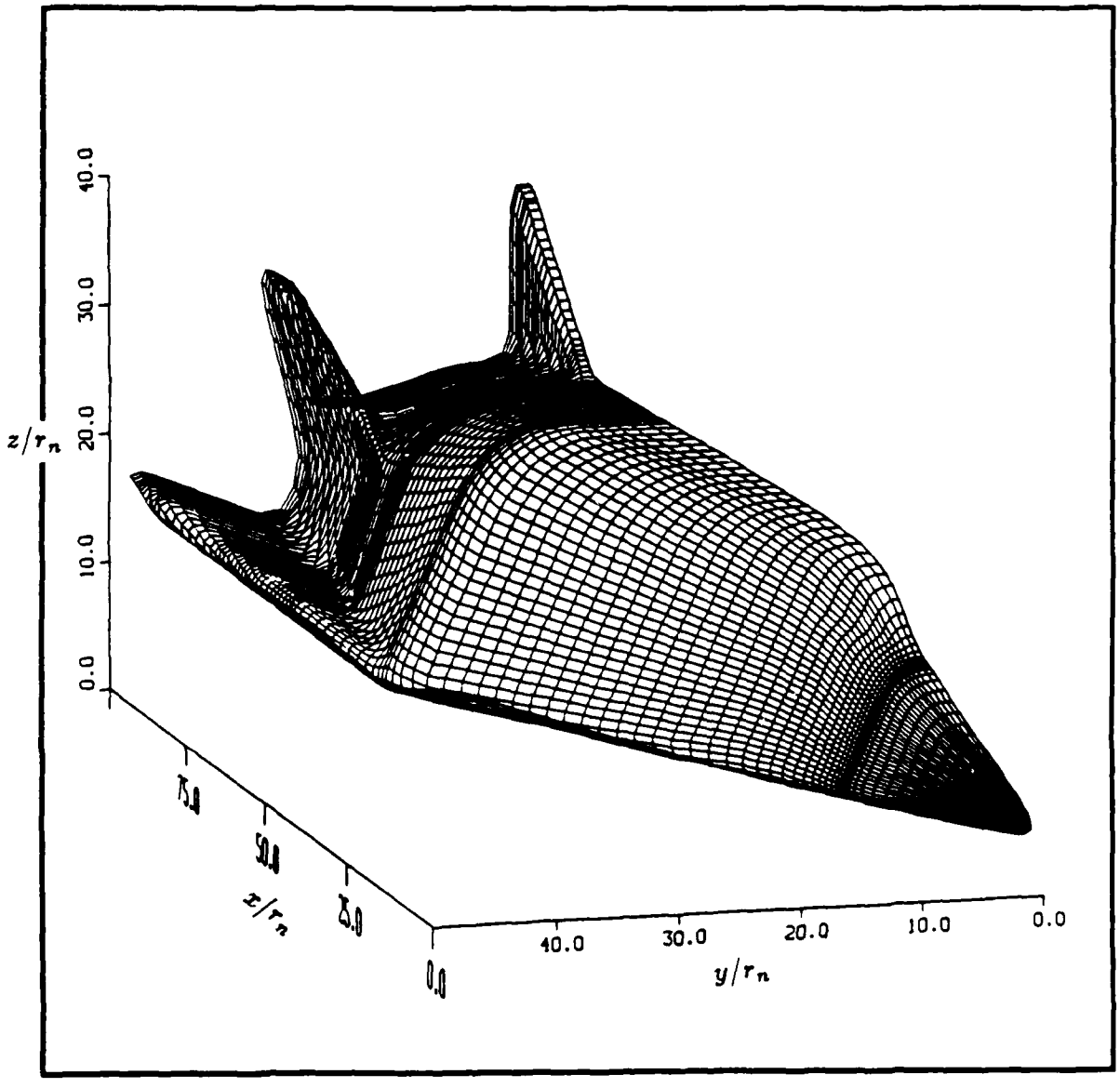

Figure 8. **X24C Body Surface**

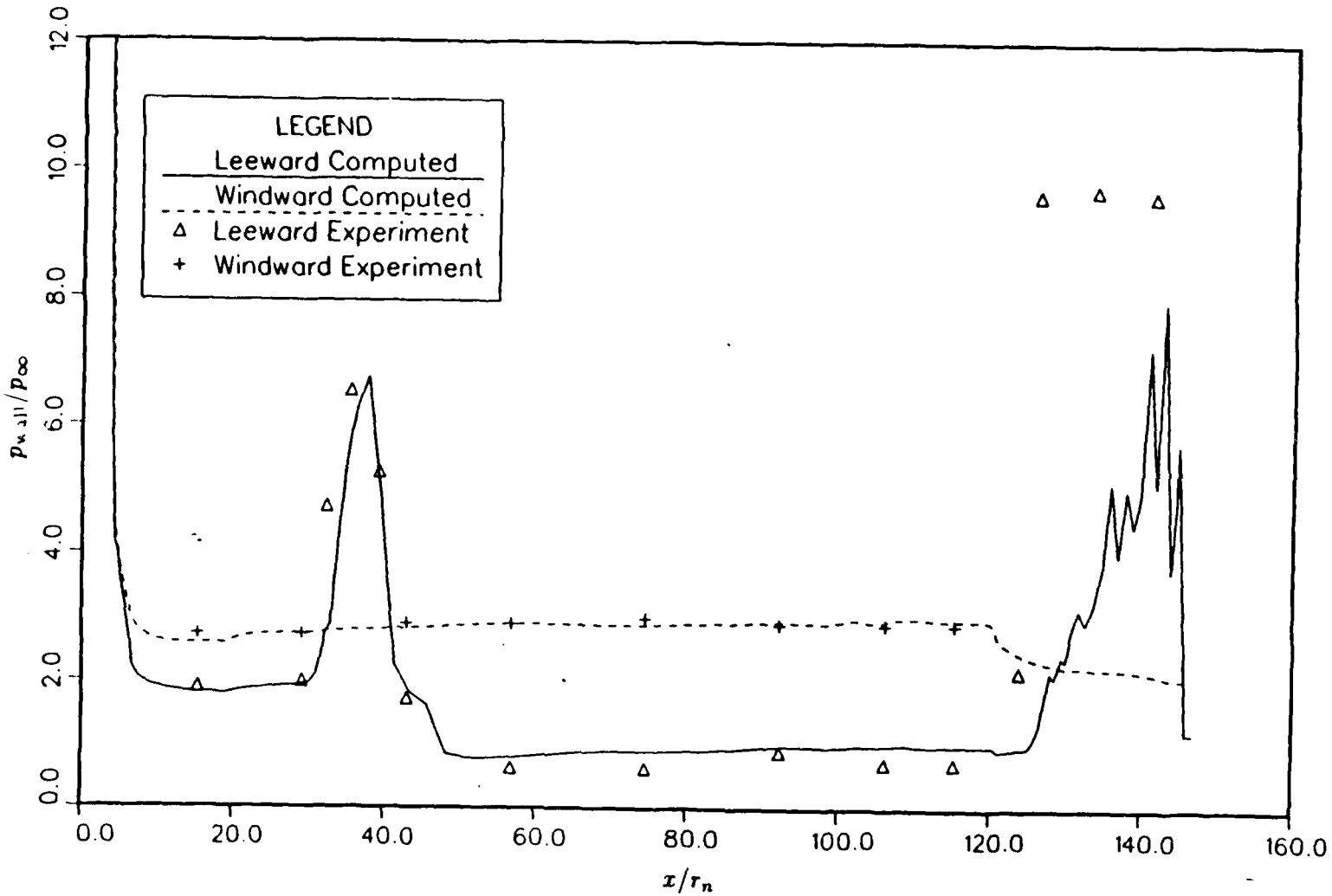

Figure 9. **Surface Pressure Distribution on Plane of Symmetry for X24C.** Experimental results from Wannernwetsch[9]. $\alpha = 6.0°$, $M_\infty = 5.95$, $Re = 16.4 \times 10^6$/m.

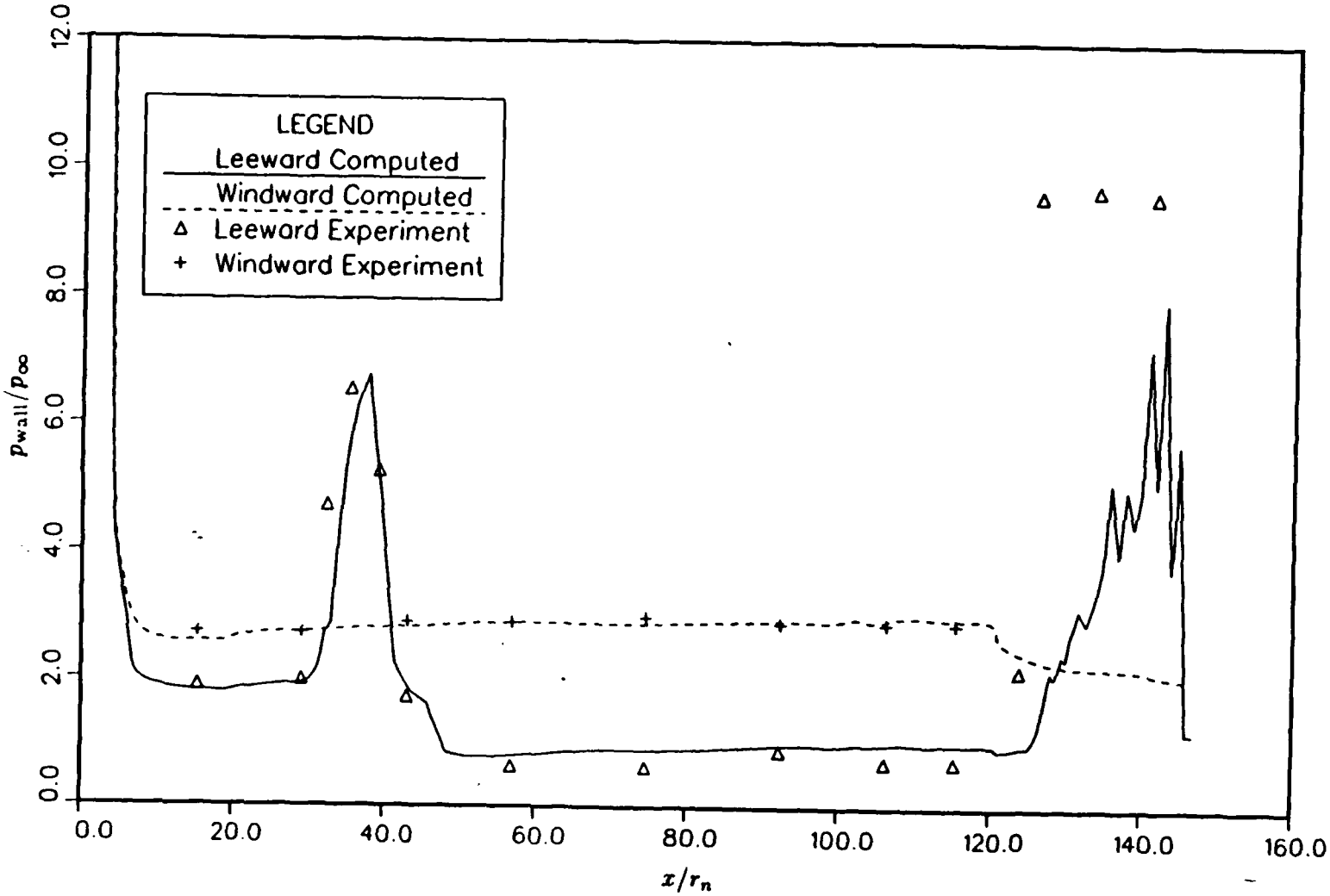

Figure 9. Surface Pressure Distribution on Plane of Symmetry for X24C. Experimental results from Wannernwetsch[9]. $\alpha = 6.0°$, $M_\infty = 5.95$, $Re = 16.4 \times 10^6$/m.

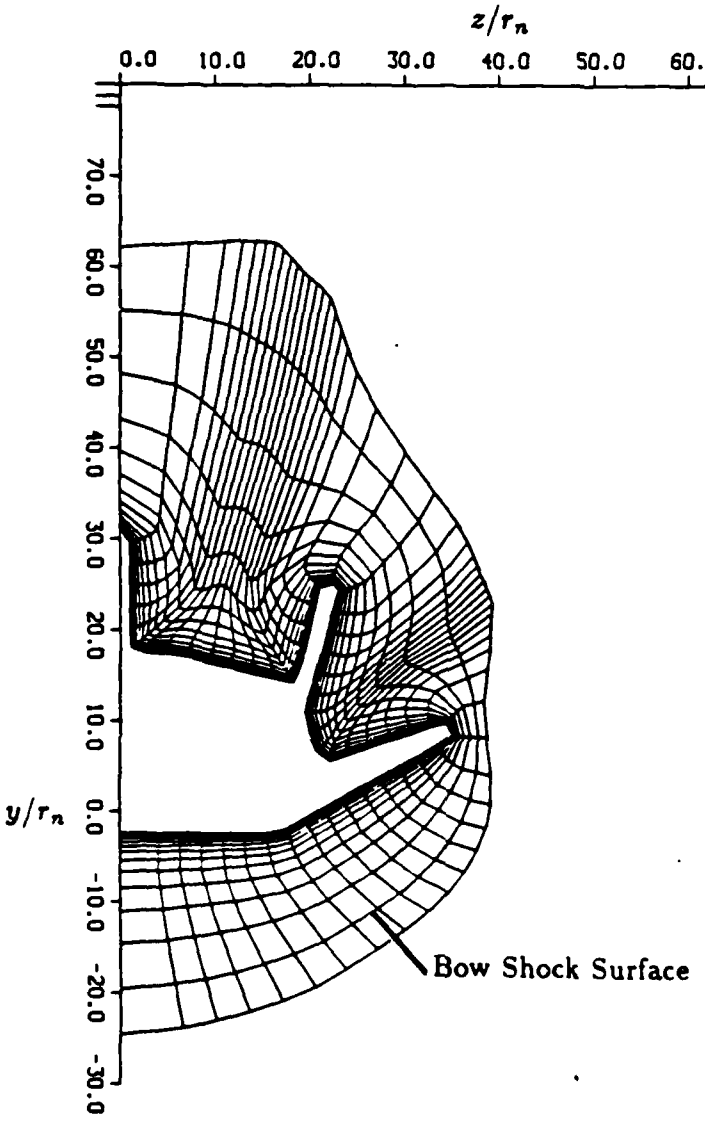

Figure 10. Computational Mesh for X24C at Plane $x/r_n = 145$
$\alpha = 7.0°$, $M_\infty = 7.97$, $Re = 1.2\times10^8$/m.

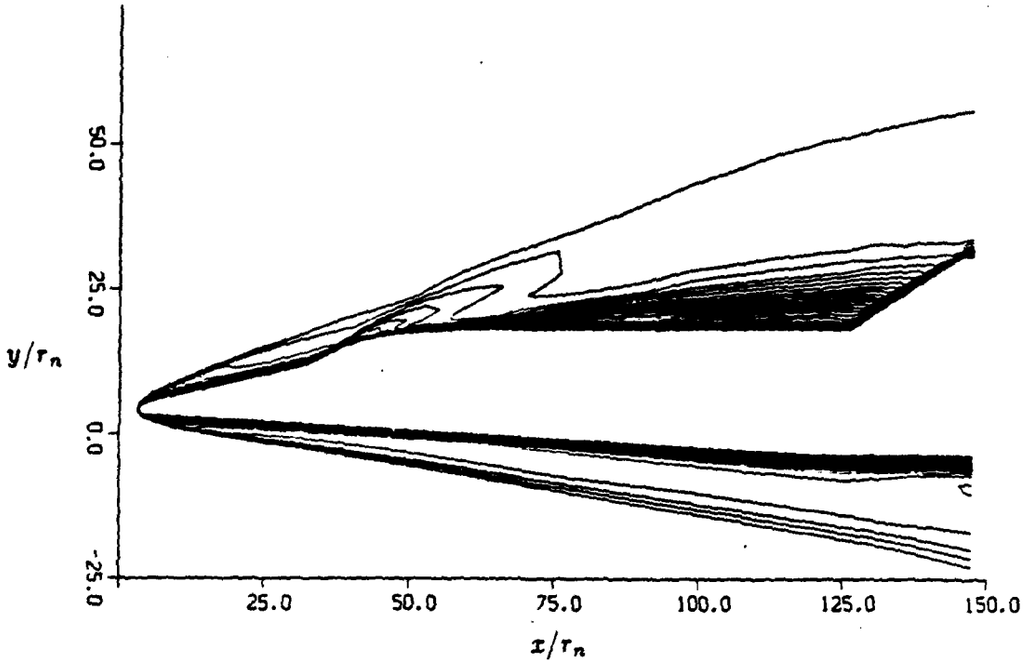

Figure 11. Mach Number Contours on Plane of Symmetry for X24C Body. $\alpha = 6.0°$, $M_\infty = 5.95$, $Re = 16.4 \times 10^6/\text{m}$.

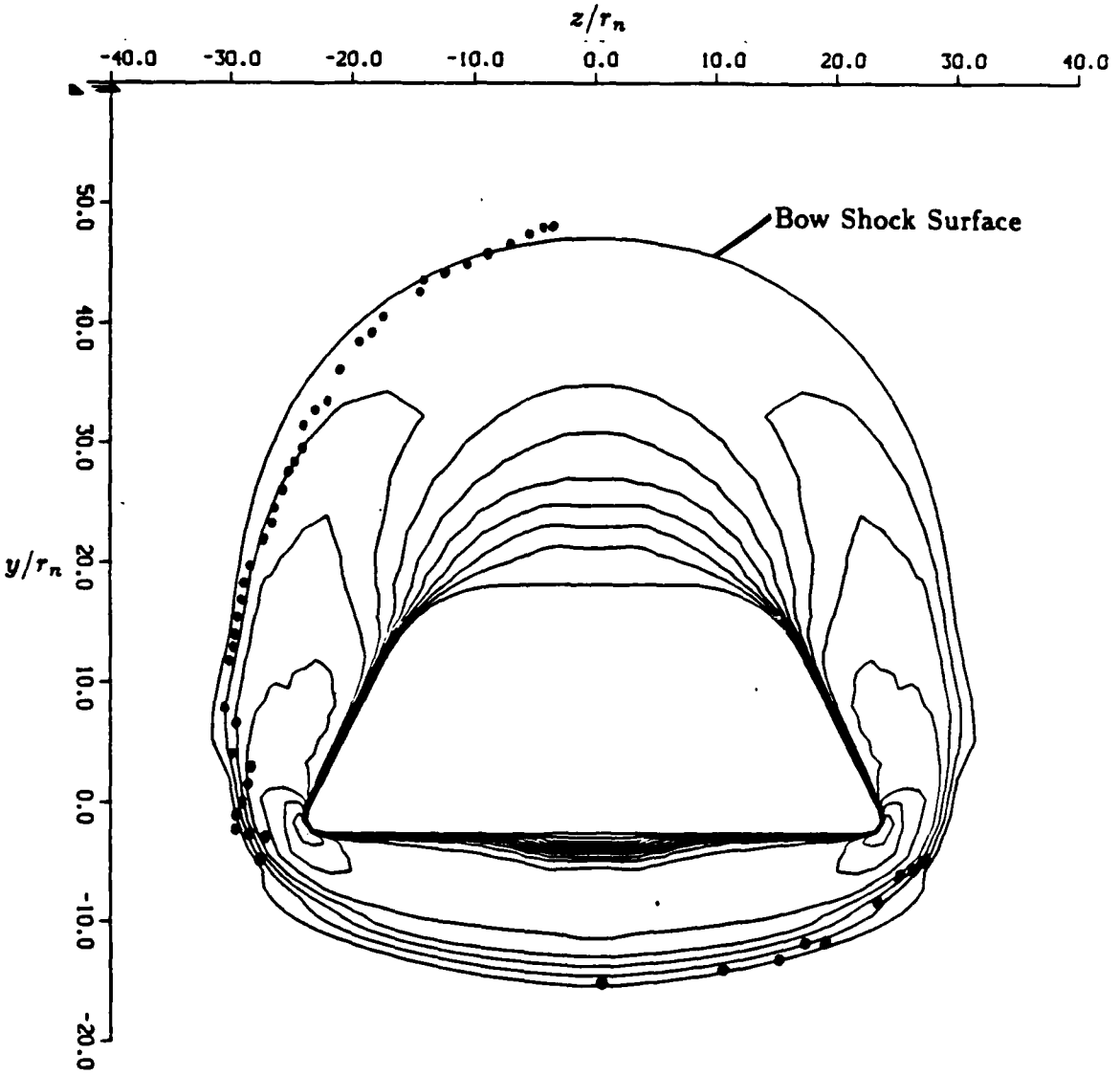

Figure 12. **Pitot Pressure Survey at x/r_n = 108 with Shock Wave Location Comparison for X24C Body.** (Outer contour of pitot pressure represents the shock wave.) Experimental results from Carver[10].
$\alpha = 6.0°$, $M_\infty = 5.95$, $Re = 16.4 \times 10^6$/m.

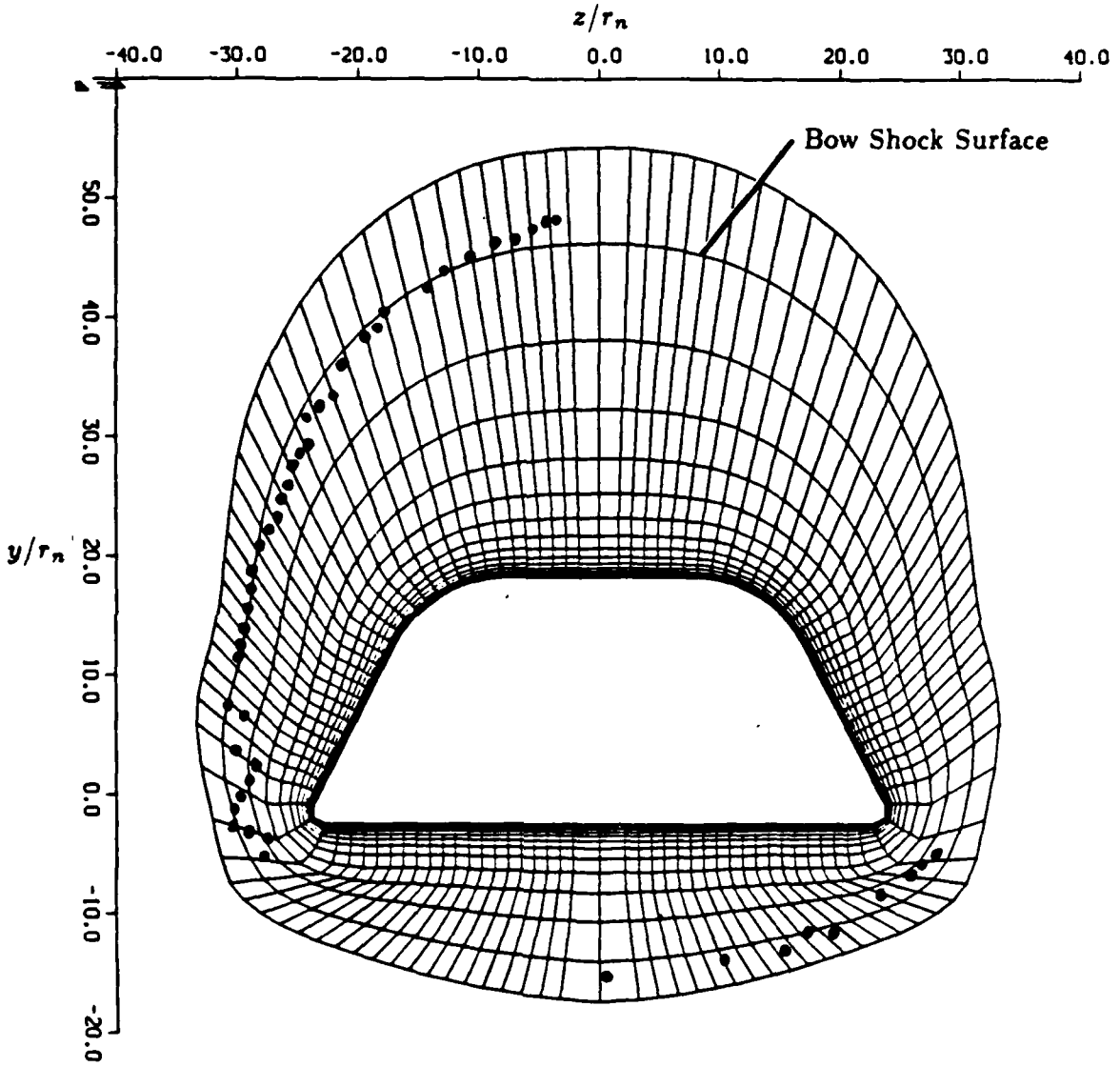

Figure 13. **Computational Mesh at x/r_n = 108 With Shock Wave Location Comparison for X24C Body.** Experimental results from Carver[10] $\alpha = 6.0°$, $M_\infty = 5.95$, $Re = 16.4 \times 10^6$/m.

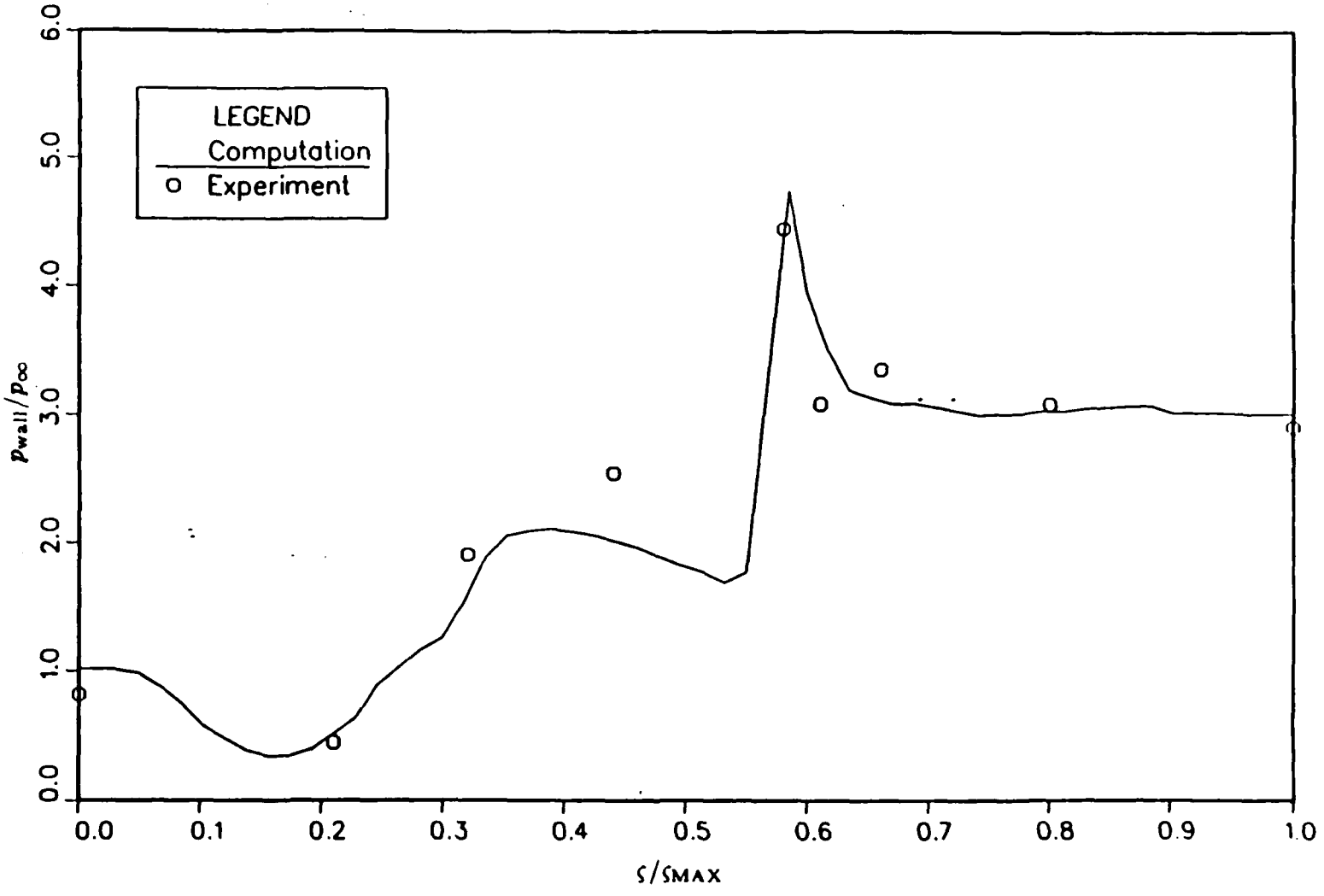

Figure 14. Surface Pressure Distribution on X24C at $x/r_n = 108$. Experimental results from Wannernwetsch[9]. $\alpha = 6.0°$, $M_\infty = 5.95$, $Re = 16.4 \times 10^6/m$.

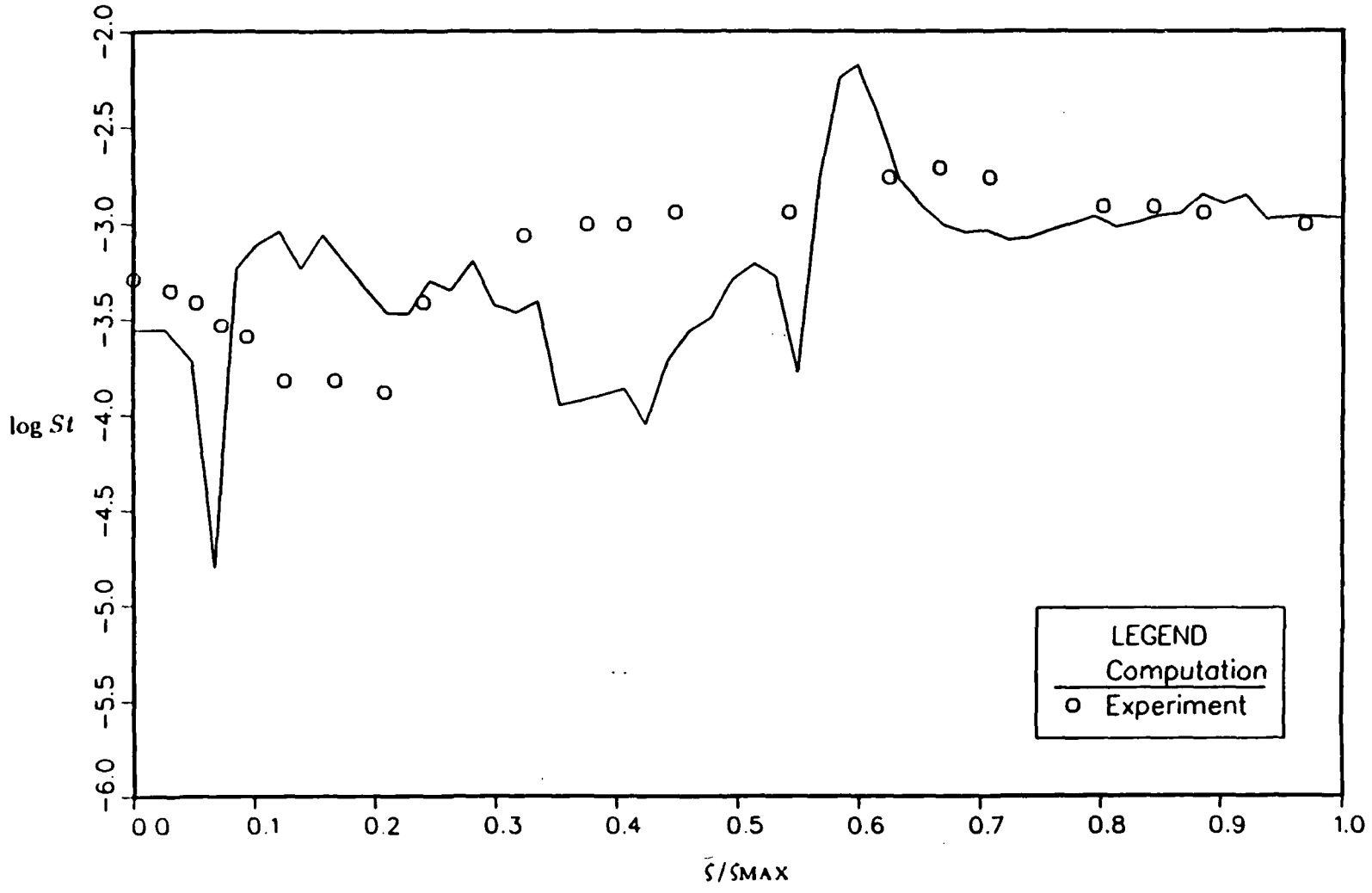

Figure 15. **Heat Transfer Distribution on X24C at $x/r_n = 108$. Experimental results** from Wannernwetsch[9] and Neumann[11]. $\alpha = 6.0°$, $M_\infty = 5.95$, $Re = 16.4\times10^6$/m.

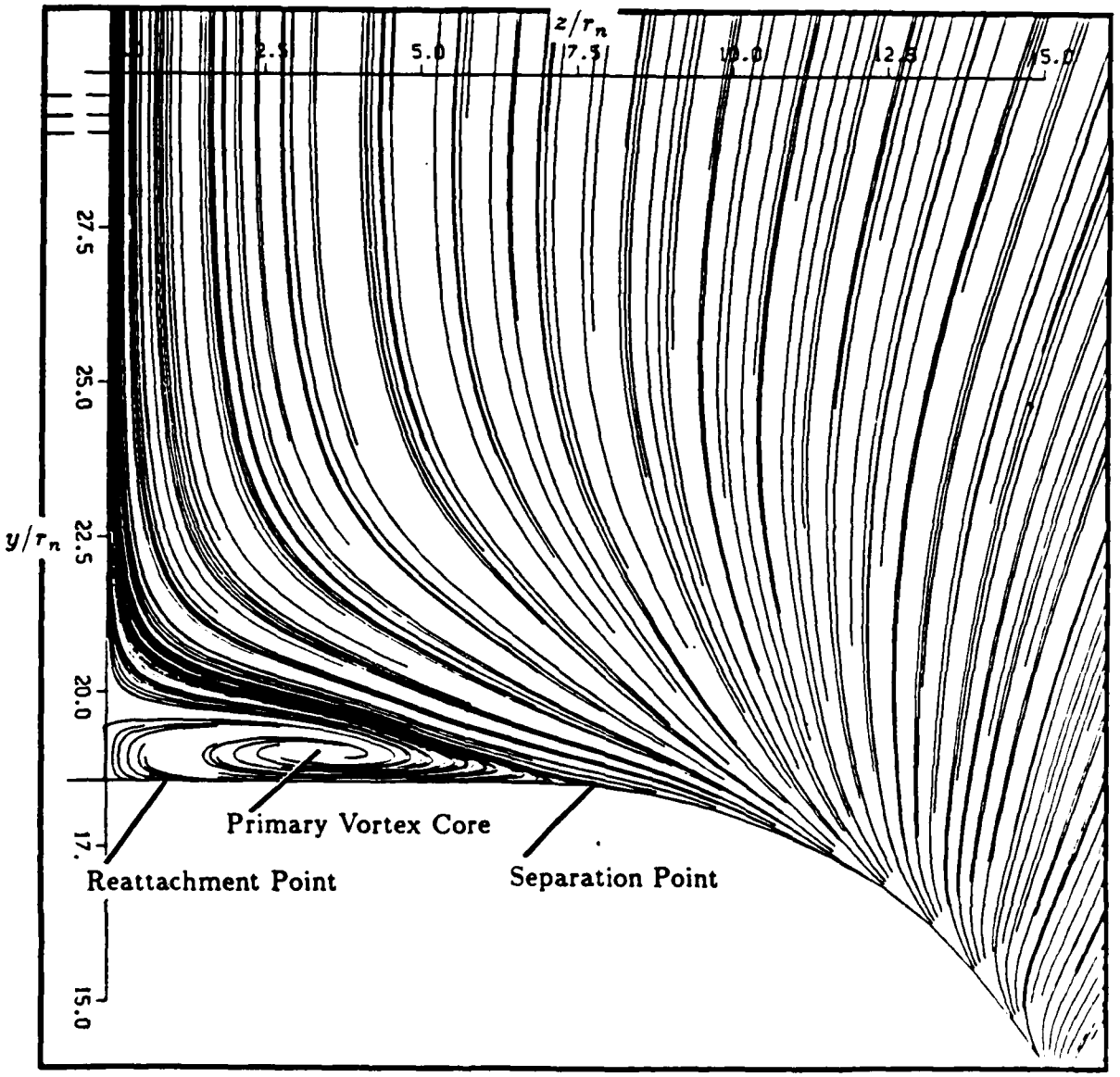

Figure 16. Streamline Traces on Leeward Surface of X24C at $x/r_n = 108$. $\alpha = 6.0°$, $M_\infty = 5.95$, $Re = 16.4 \times 10^{6}$/m.

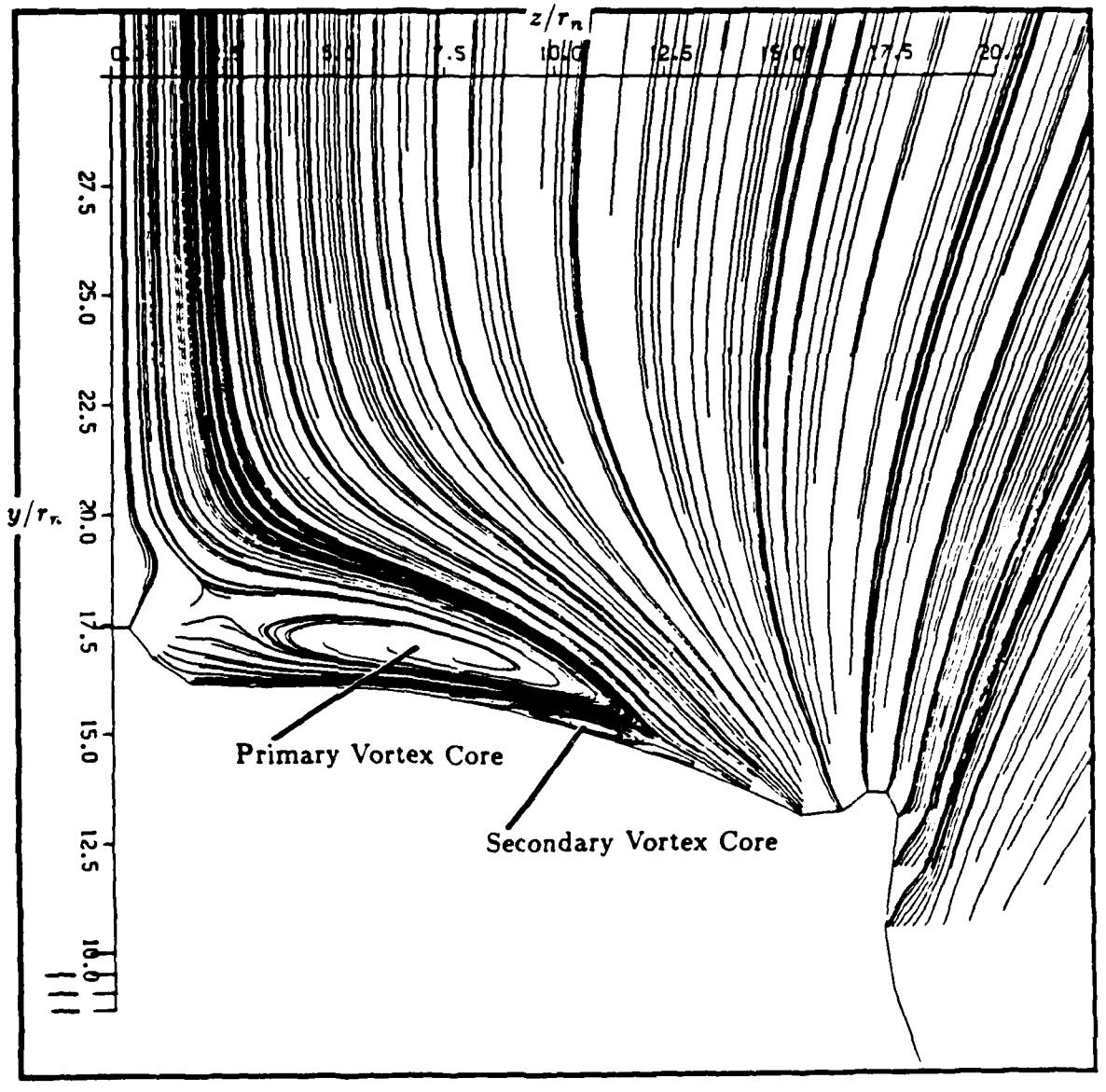

Figure 17. Streamline Traces on Leeward Surface of X24C at $x/r_n = 127.5$, $\alpha = 6.0°$, $M_\infty = 5.95$, $Re = 16.4 \times 10^6$/m.

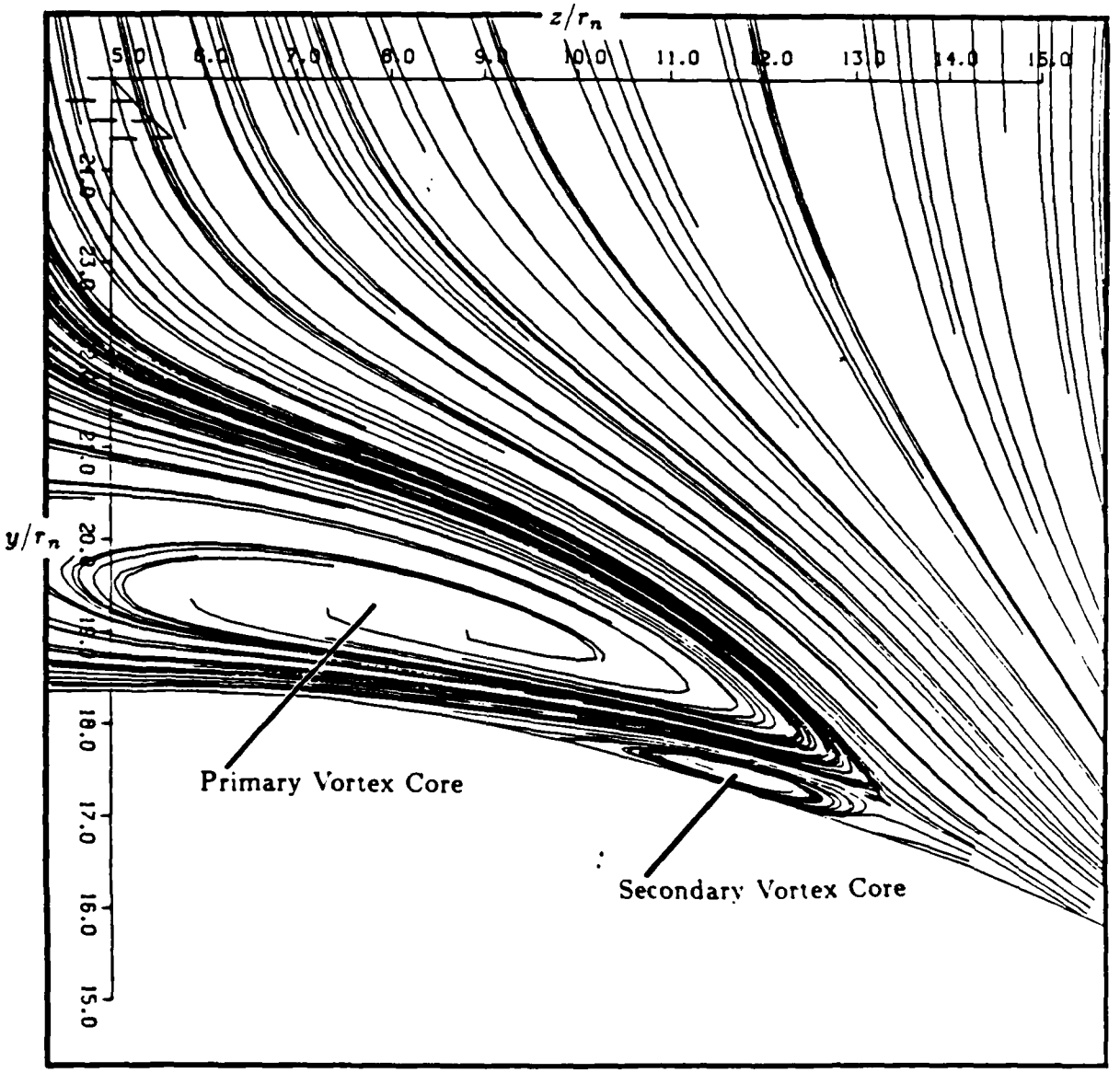

Figure 18. Enlargement of Streamline Traces on Leeward Surface of X24C at x/r_n = 127.5. α = 6.0°, M_∞ = 5.95, Re = 16.4 × 10^6/m.

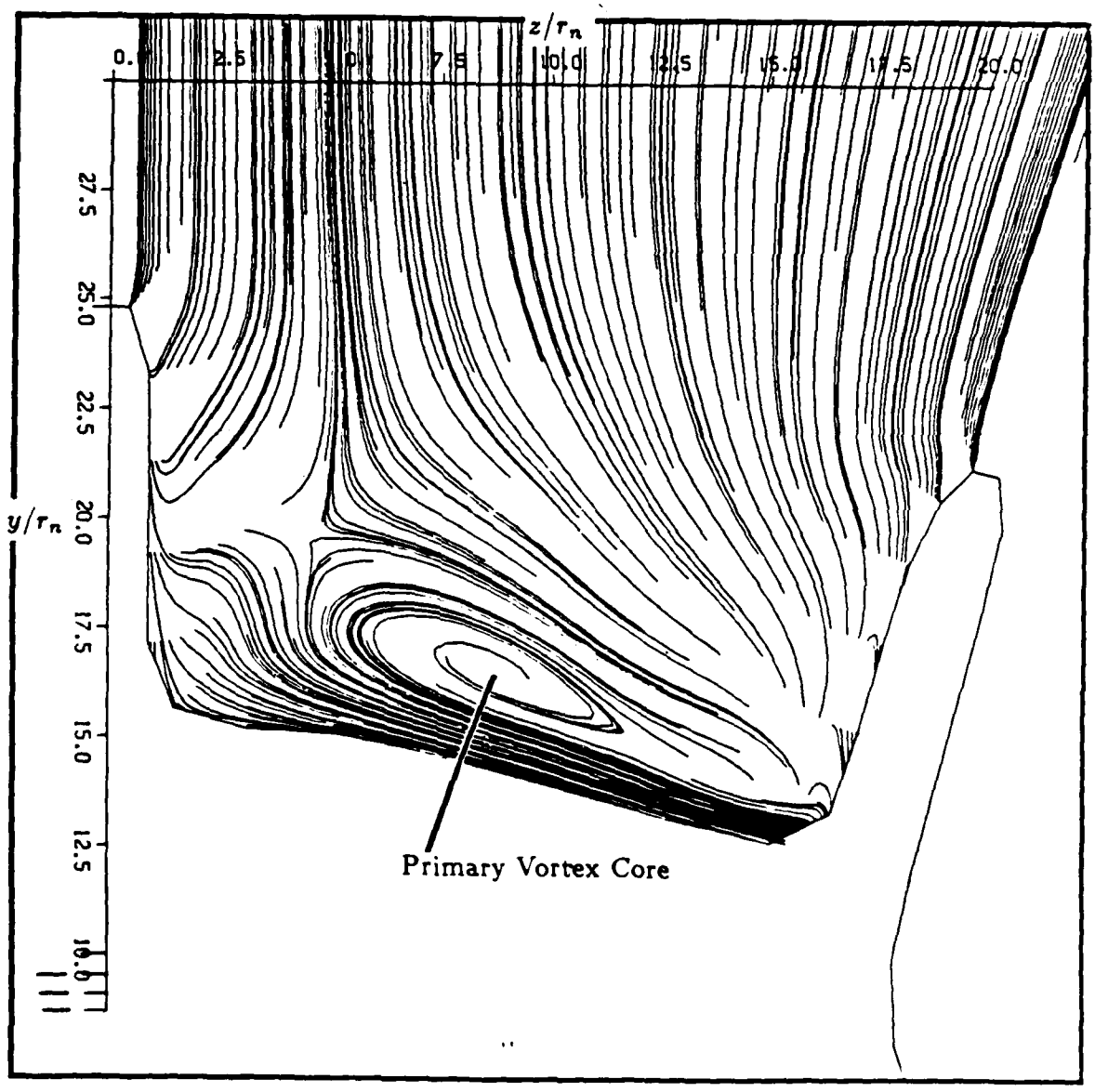

Figure 19. Streamline Traces on Leeward Surface of X24C at $x/r_n = 140$. $\alpha = 6.0°$, $M_\infty = 5.95$, $Re = 16.4 \times 10^6$/m.

END

1-87

DTIC